JAERI-Research
99-011

THE EVALUATION OF RADIATION DAMAGE TO THE TARGET MATERIAL DUE TO THE INJECTION OF MEDIUM- AND HIGH-ENERGY PROTON

March 1999

Hiroshi TAKAHASHI*, Xinji CHEN*,
Toshinobu SASA and Takakazu TAKIZUKA

日本原子力研究所
Japan Atomic Energy Research Institute

本レポートは、日本原子力研究所が不定期に公刊している研究報告書です。
入手の問合わせは、日本原子力研究所研究情報部研究情報課（〒319-1195　茨城県那珂郡東海村）あて、お申し越し下さい。なお、このほかに財団法人原子力弘済会資料センター（〒319-1195　茨城県那珂郡東海村日本原子力研究所内）で複写による実費領布を行っております。

This report is issued irregularly.
Inquiries about availability of the reports should be addressed to Research Information Division, Department of Intellectual Resources, Japan Atomic Energy Research Institute, Tokai-mura, Naka-gun, Ibaraki-ken 319-1195, Japan.

編集兼発行　日本原子力研究所

The Evaluation of Radiation Damage to the Target Material Due to the Injection of Medium- and High-Energy Proton

Hiroshi TAKAHASHI*, Xinji CHEN*, Toshinobu SASA and Takakazu TAKIZUKA

Center for Neutron Science
Tokai Research Establishment
Japan Atomic Energy Research Institute
Tokai-mura, Naka-gun, Ibaraki-ken

(Received January 26, 1999)

In the Japanese OMEGA program, the accelerator driven transmutor has been studied for eliminating the minor actinide using the fast neutron deep subcritical reactor. In this system, radiation damage to the structural materials by neutrons and charged particles is more severe than in an ordinary fission reactor. It is very important to estimate radiation damage to the transmutor because the damage primarily determines the life of the materials. The damage to the structural materials was investigated using Monte Carlo simulation codes LAHET, HMCNP, and HTAPE. Atomic displacement (DPA), H and He production rates, and energy deposition were evaluated. In calculating the DPA cross section, the TRANSX2 code was used. By using these values, we calculated the radiation damage and heat deposition of the system. It requires the frequent replacement of target or beam window and results into the low plant factor. By choosing the smaller subcriticality, this difficulty can be avoided. Otherwise we need the search for materials which has the low DPA cross section.

Keywords: Accelerator-driven System, Transmuter, Minor Actinide, Radiation Damage, Atomic Displacement, Hydrogen Production, Helium Production

---

This work was supported by Japan Atomic Energy Research Institute and U.S. Department of Energy at Brookhaven National Laboratory under Contract No. DE-AC02-76CH00016.

* Brookhaven National Laboratory

中高エネルギー陽子入射によるターゲット材の照射損傷の評価

日本原子力研究所東海研究所中性子科学研究センター
高橋　博*・Xinji CHEN*・佐々　敏信・滝塚　貴和

(1999年1月26日受理)

日本のオメガ計画では、高速未臨界炉心を用いてマイナーアクチノイドを消滅する加速器駆動消滅炉が研究されている。このシステムでは、構造材への中性子と荷電粒子による放射線損傷が既存の核分裂炉よりも深刻な問題となる。消滅炉の放射線損傷を評価することは、損傷が主として材料の寿命を決定するため、特に重要である。構造材の損傷はモンテカルロシミュレーションコードLAHET, HMCNP及びHTAPEを用いて検討した。そのため、原子の弾き出し(DPA)、水素、ヘリウムの生成率及びエネルギー損失が評価された。DPA断面積の計算にはTRANSX2コードを使用した。これらの値を使用して、システムの放射線損傷と発熱密度を計算した。ターゲットやビーム窓の頻繁な交換は、システムの稼働率を低下させる可能性があるが、浅い未臨界度を選択すればこの問題は解決される。一方で小さいDPA断面積を持つ構造材の調査も必要である。

本研究は契約番号DE-AC02-76CH00016の下で、日本原子力研究所と米国エネルギー省の支援によりブルックヘブン国立研究所で行われた。
東海研究所：〒319-1195　茨城県那珂郡東海村白方白根２－４
* ブルックヘブン国立研究所

Contents

目　次

1. Introduction

In the Japanese OMEGA program, the accelerator-driven transmutor has been studied for eliminating the minor actinide using the fast neutron deep subcritical reactor. The fast reactor with hard neutron spectrum is effective to transmute minor actinides, because the minor actinide nuclei can be fissioned by high energy neutrons. However, it is not advisable to run the fast reactor with hard neutron spectrum in the critical condition, because of the positive Na void coefficient, short neutron life time, smaller delayed neutrons portion and small doppler coefficient which are associated with the hard neutron spectrum The critical safety problem becomes serious. To avoid the positive Na void coefficient, the small or flattened core, which is not neutron economical, has been adopted.

When a reactor is run in a subcritical condition by providing spallation neutrons, the safety problem associated with the criticality can be alleviated without sacrificing the neutron economy[1]. In the Japan Atomic Energy Research Institute (JAERI), accelerator-driven transmutor of minor actinide[2], rather deep subcriticality of k =0.90 is adopted to avoid the recriticality which might occurs when the core meltdowns.

In the accelerator-driven transmuter, high-energy, high-flux neutrons are produced by the spallation reaction, and these spallation neutrons, as well as fission neutrons from the core, are used to transmute the radioactive wastes[1-3]. In such a system, radiation damage to the structural materials by neutrons and charged particles is more severe than in an ordinary fission reactor. It is very important to estimate radiation damage to the transmuter because the damage primarily determines the life of the materials.

We studied radiation damage to a JAERI transmutation system driven by a proton accelerator. The transmuter is composed of a tungsten target, beam window, structural wall, subcritical core, and reflector. Because of the rather deep subcriticality, the proton accelerator power is high and it results in the high radiation damage. The spallation neutrons, as well as

the fission neutrons, cause the radiation damage. We evaluated the atomic displacement, the production rates of hydrogen and helium, and energy deposition. The fuel is Na-cooled pin-bundle metal fuel that contains minor actinides (MAs). The tungsten target and beam window recurred large damages. The structural wall near the beam window also had a large atomic displacement when the proton beam power is large for large subcritical reactor. This suggest that the small subcriticality which requires the small proton power is desirable beside of the flatter power distribution.

2. Geometry and Material Composition of the Transmuter

Figure 2.1 shows the r-z cross sections of transmuters that use the spallation reaction generated by medium energy protons[4, 5]. The tungsten target is a cylinder with radius of 10 cm and assumed to be bombarded with a homogeneous proton beam with a 3 cm radius. The beam windows are made of stainless steel (Fe 87 % and Cr 13 % : these values are representative of stainless steel), 0.5 cm thick, and a density of 6.24 g/cm^3. The 2 cm-thick structural walls between the core and the lead target are made of the same stainless steel as the beam window.

The fuel is the metal pin-bundle fuel that contains minor actinides (MAs) and tungsten. The material compositions of each regions are shown in the table 2.1 and 2.2. The length of the core was fixed at 140 cm, its outer and inner radius are respectively 70 cm and 20 cm. The core was surrounded by a reflector made of stainless steel whose composition was the same as that of the beam window. The outer radius of the reflector was 130 cm, and its length was 220 cm.

3. Calculational Methodology

The nucleon meson transport process above 20 MeV nucleon and 150 MeV pion are calculated with the nuclear cascade process code system LAHET which has been assembled and developed at LANL from NMTC, HETC, and ISABEL codes. This LAHET code treats all the interactions by protons, and pions, but only treats neutron interactions above a cutoff energy, 20 MeV. And neutron transport under 20 MeV is calculated by the Monte Carlo code HMCNP[8] using the neutron source generated by the LAHET code. The information on secondary particles is written on a history file. By running the HTAPE code[7, 8] that uses the history file as an input, we obtained the neutron flux, production rates of H and He, and energy deposition.

The tungsten target, structural walls, and the core were divided into small cells to estimate the positional dependence of the radiation damage. The atomic displacement was calculated by multiplying the neutron flux with the atomic-displacement cross section. The neutron flux of neutron energy below 20 MeV was calculated with the HMCNP code, while that above 20 MeV was obtained by the HTAPE code. The atomic-displacement cross section (DPA = Displacements Per Atom) at neutron energy below 20 MeV was obtained from MATXS library, using the TRANSX2 code[9]. However, above 20 MeV, no atomic-displacement cross section was available. For stainless steel, the DPA cross section at energies above 20 MeV was obtained from Dr. Yu.A. Korovin[10, 11]. Figure 3.1.1 shows the DPA cross section of stainless steel for neutron energies between 20 and 800 MeV referred to by Korovin et al.; the cross section is nearly constant in this energy range. Accordingly, we assumed that the DPA cross sections other than that of stainless steel, such as tungsten target and the core, were constant above 20 MeV, and were equal to the values at 20 MeV obtained by the TRANSX2 code.

In Figs. 3.1.1-3.1.7, we show the DPA cross sections of stainless steel, tungsten target, and the cores. Compared to the lead target, the DPA cross section in the tungsten

target is large in the energy range of 2 eV -100 eV. Due to this large DPA cross section makes larger DPA than the lead target. Thus, the tungsten target requires more frequent replacement than the solid lead target although there is advantage of the little high spallation yield in the tungsten target. In Figs.3.2.1-3.2.6 we show the (n, p) cross sections for tungsten 1st and 2nd target, material for and fuel (core), radial and axial reflector regions.
In Figs.3.3.1-3.3.6, we show the cross section of (n, a) for the all materials.

4. Results and Discussion

The multiplication factor calculated using the option of criticality in HMCNP code is 0.955. The number of the spallation neutrons which generated in the reaction of the nucleon energy larger than 20 MeV is 20 which is larger than the multiplication calculated from criticality calculation option in the HMCNP code.

4.1 Neutron Spectrum

The neutron fluxes which are normalized to one incident proton are shown in the following figures. The high-energy neutron flux is high in lead target cell #5 compared with other cells. Neutron spectra in the core # 11,12, 13 and the radial reflector #23 are shown in the Figs 4.1.1-4.1.4 The neutron spectrum becomes softer in the order of cell #11 12 13 and 23. The spallation neutrons which energy are more than 10 MeV are in the radial reflector regions.

The ratios of neutron fluxes with energies above 20 MeV and below 20 MeV are less than 10^{-2} in cells, such as #31,32,41, and #45, that are largely influenced by the proton beam. In other cells such as core and reflector regions, the ratios become much smaller than these values.

4.2 Table of the Annual Atomic Displacement (DPA), Energy Deposition, and H and He Production Rates

Tables 4.1 shows the annual atomic displacement (DPA), energy deposition, and H and He production rates of each cell in the case of the 10 mA proton beam current. The total thermal power becomes 456 MW at this beam current. To get nominal thermal power output of 600 MW in JAERI's design, the proton beam current should be increased to 600MW/456MW* 10mA = 12.3 mA. And the radiation damage of DPA, energy deposition, etc. increase proportionally to the beam currents.

Our beam current required to run 600 MW thermal power is much smaller than the beam current which is obtained in JAERI's design. The reason of this is due to the fact that the multiplication factor calculated here is 0.955 instead of the 0.90 at JAERI's one.

4.3 DPA

Highest DPA value are 149/year in the core region #11. at this region DPA =59.6, it is estimated that maximum DPA which can be allow the stainless steel (SS) material is about 130, thus every year the core fuel needs replacement. The window section has 40.3 it can stand about 3 year for 10 mA beam, the target section in the half upper section #31-33 is about the 44. which are very close to the window's DPA. Beyond this depth value, the DPA in the target wall has little higher than those in the target section, so that if target diameter is small, the damage of the target wall is high and the frequent replacement might be required.

The DPA is depend on the proton beam currents, the high current proton beam requires in the deep subcritical system as shown in the analysis of the lead target for particle fueled reactor and fast reactor.

When the subcriticality is not large, the proton beam current can be small, then the atomic displacements become larger in the core cells mainly influenced by fission neutrons,

and also in the target cells regions,

As shown in Figs.3.1.3, 3.1.6 and 3.1.7 in the core and target, the DPA cross sections have large resonance behavior in the range of neutron energy between 20 eV to 100 eV. The large neutron fluxes in this energy range contribute these large DPA.

4.4 Heat Deposition

The energy deposition due to high energy reaction is the largest in the stainless steel window #41 390.3 watt/cc. The second largest is in the target section cell #33 298.5 watt/cc, this is larger than the front parts of target cell #31 and #32 where the deposition are respectively 259.7 and 199.5 W/cc. This peak value at cell #33 correspond to the Bragg peak in the target. The heat depositions in the core region are comparable to the one of the target regions. This is mostly due to the fission reaction. The highest heat deposition by fission reaction in core is 294.W/cc, and the one by the high energy reaction is only 1.64 W/cc. The peaking factor of this small non-flat reactor is not so large.

The wall region of target are much smaller than the target regions. This is due to the small cross section of deposition energy in the stainless steel compared to the tungsten materials.

Their energy depositions are quite high, therefore, an effective cooling system should be considered. However, if a slightly subcritical transmuter is used, the energy deposition in the target region becomes smaller than this calculation because of a low proton beam current.

4.5 Hydrogen Production

In general, hydrogen is deposited in the system by the spreading of the proton beam arising from multiple Coulomb scattering. Hydrogen is also deposited by secondary protons generated mainly in the lead target that are slowed during their transport, as well as by

secondary protons produced by (n, xp) or (p, xp) reaction, and deuterons through evaporation. Highest hydrogen production occurs at window region, second highest production region is in the cell #33. similar to the heat deposition and DPA the hydrogen production in the frontal parts in the cell 31 and 32 are smaller than the value in cell #33 behind this cells of #34 and #35 is reduced rapidly, In the target wall region of cell #45 and #44 are factor 3 smaller than the target region. Region which are far way from target becomes very small.

4.6 Helium Production

Helium is generated by an evaporation process caused by nuclear interactions. The tungsten cell #31 and the stainless beam window cell #41 respectively have He production rates of $1.5*10^{-4}$, and $8.3*10^{-5}$ mol/cc/yr, because they are directly effected by the proton beam. The He production rate is 74% less than the H production rate in cell #31, while it is ~4 % in cell #41. The H and He production rates in cell #44 (the structural wall near the beam window) are not as large, unlike the large DPA in this cell. Generally, a higher proton beam current gives larger H and He production rates.

5. Comparison with the Radiation Damage of Accelerator-driven Fast Reactor with Particle Fuel (PFT) and MOX Fuel (MFT)

We studied radiation damage of accelerator-driven fast reactor with particle fuel (PFT) and MOX fuel (MFT) in the previous work. The target is lead instead of tungsten, and there is no tungsten in the core. As mentioned in the above, the tungsten has large DPA cross section in the energy range between 2 - 100 eV, so that the DPA in the core is quite large in the JAERI's transmutor. But the transmuters without tungsten in the core has highest DPA in the target and surrounding target vessels. Since this is depend on the incident proton currents, we reiterate the main results of analyzing these two transmuters in this section.

To study the effects of the proton current intensity on the radiation damage, we analyzed the transmuters with particle fuel (PFT) and MOX fuel (MFT) were studied by varying the thickness of core, in other words, the k_{eff}.

Figure 5.1 shows the r-z cross sections of transmuters that use the spallation reaction generated by high energy protons[4, 5]. The centers of the cylinders are made of lead targets with a radius of 8 cm and density of 11.34 g/cm^3. It is assumed that the target is bombarded with a homogeneous proton beam of energy 1 GeV with a 3 cm radius. The beam windows are made of stainless steel (Fe 87 % and Cr 13 %: these values are representative of stainless steel), 0.5 cm thick, with a radius of 8 cm, and a density of 6.24 g/cm^3. The 2 cm-thick structural walls between the core and the lead target are made of the same stainless steel as the beam window.

Two types of fuel in core were investigated; one was a He-cooled particle fuel that contains minor actinides (MAs), and the other was a Na- cooled mixed oxide (MOX) fuel. The composition of the particle fuel is the same as that studied by Mukaiyama et al.[6]. For the MOX fuel, the Pu enrichment was 20.0 w/o for the inner core and 27.6 w/o for the outer core. The weight fraction of Pu was ^{239}Pu: ^{240}Pu: ^{241}Pu: ^{242}Pu = 58: 24: 14: 4 (w/o).

The length of the core was fixed at 120 cm, but its outer radius was varied from 60 cm to 20 cm to change the k_{eff} of the system. The core was surrounded by a reflector made of stainless steel whose composition was the same as that of the beam window. The outer radius of the reflector was 90 cm, and its length was 180 cm. The k_{eff} for various core radii were calculated with the criticality calculation option of MCNP code[7].

The lead target, structural walls, and the core were divided into small cells to estimate the positional dependence of the radiation damage (Fig.5.1). The length in the z-direction of cells #5-8 and #10-15 is 30 cm. The core was divided into three cells of the same length in the r-direction. For the particle fuel transmuter (PFT), cells #1-3 have the same composition, but for the MOX fuel transmuter (MFT), cells #1 and #2 have the inner-core composition (20

w/o Pu enrichment), and cell #3 has the outer-core composition (27.6 w/o Pu enrichment).

The total powers of the PFT and MFT were assumed to be 1000 MW_{th} and 700 MW_{th}, respectively, when the outer radius of the core was 60 cm; in other words, R in Fig. 5.1 was 50 cm. When we reduced the outer core radius to decrease the k_{eff} the transmuter, we also reduced the total power so that the transmuter had a constant power density (760 W/cm^3 for PFT and 530 W/cm^3 for MFT). We assumed that the proton beam energy was 1 GeV. From the results of the energy deposition per proton calculated by HTAPE and HMCNP codes, we established the proton beam current so that the transmuter had the desired power.

In Figs. 5.2.1-5.2.5, 5.3.1-5.3.5 and 5.4.1-5.4.5 we show respectively the cross sections of DPA, (n,p), and (n, a) for stainless steel, lead, and the cores.

Figures 5.5.1 and 5.5.2 show the effective multiplication factors (k_{eff}) of PFT and MFT, respectively, as a function of the core thickness (R) in the radial direction. The k_{eff} increases monotonically as R increases. In the case of $k_{eff} < 1$ where an accelerator is needed to operate the transmuter, we chose R = 10 and 20 cm for PFT, and R = 10, 20, and 30 cm for MFT, and calculated the radiation damage for each case. From the results of the HMCNP and HTAPE calculations, we obtained the energy deposited in the system by one proton. Then, we evaluated the proton beam current, taking into account the total power of the transmuter.

Tables 5.1 and 5.2 show the annual atomic displacement (DPA), energy deposition, and H and He production rates of each cell for PFT and MFT with different Rs, together with k_{eff}, the total thermal power, and the proton beam current required. The atomic displacement is the severest in lead cell #5, because this cell is influenced most by the incident proton beam and the spallation neutrons produced by protons. The beam window (cell #9) has the second largest atomic displacement, because this cell is bombarded directly with the proton beam. We notice that the cell #12 of the structural wall also has a large atomic displacement. When the k_{eff} is smaller and the proton beam current is higher, cells #5, #9, and #12 that are largely influenced by the proton beam have larger atomic displacements; when the k_{eff} is

larger and the proton beam current is lower, then the atomic displacements become larger in the cells mainly influenced by fission neutrons, such as cells #1, #2, and #3.

The DPA caused by neutrons with energies above 20 MeV is smaller than that caused by neutrons with energies below 20 MeV, although the DPA cross section above 20 MeV is larger than that below 20 MeV. This difference is because the neutron flux with energy below 20 MeV is dominant. The ratios of neutron fluxes with energies above 20 MeV and below 20 MeV are a few percent even in cells, such as #5, #9, and #12, that are largely influenced by the proton beam. In other cells, the ratios are below 1%. Figs. 5.6.1-5.6.7 and 5.7.1-5.7.7 show the neutron spectra in various cells in PFT and MFT, respectively. The neutron flux is normalized to per proton, and is divided by the lethargy of each energy bin in HMCNP and HTAPE. Furthermore, the flux is integrated over all time. Because the number of fission neutrons increase with increasing core thickness, R, the neutron flux in the energy range of 100 eV to 10 MeV becomes larger for a larger R. On the other hand, the high-energy neutron fluxes in each cell for different Rs are almost equal because the size of the lead target is fixed, and the number of neutrons produced by one proton is almost same, even if R is changed. The high-energy neutron flux is high in lead target cell #5 compared with other cells. Comparing the neutron spectra in PFT to those in MFT, we notice that PFT gives harder spectra than the latter. The fuel in the PFT core is particle fuel, mainly made of minor actinides[6]; minor actinides are apt to capture lower energy neutrons and to fission to higher energy neutrons. As a result, the neutron spectrum is harder in PFT than in MFT.

Figures 5.8.1-5.8.7 and 5.9.1-5.9.6 show the annual atomic displacement of various cells in PFT and MFT as a function of k_{eff}. The figures show the DPAs by neutrons with energies below 20 MeV and above 20 MeV, which are based on the fluxes calculated by the HMCNP and the HTAPE codes. We also show the DPA based on the fluxes calculated by the MCNP code in which we used the criticality calculation option; this DPA does not include the effect due to the spallation neutrons produced by the proton beam. The DPAs based on the results by HMCNP and by MCNP coincide, in principle, at $k_{eff} = 1$. The DPAs based on the MCNP results (solid lines in Figs. 5.8.1-5.8.7 and 5.9.1-5.9.6) increase with

increasing k_{eff} because the contribution by fission neutrons rises as k_{eff} increases. For PFT, the DPAs by neutrons below 20 MeV based on the HMCNP results (dashed lines in Figs. 5.8.1-5.8.7) in cells #9, #12, and #5 decrease as k_{eff} increases because those cells are largely influenced by the proton beam and the proton beam current decreases as k_{eff} increases. However, the DPAs in cells #1, #3, #7, and #14 increases as k_{eff} increases because, in those cells, the fission neutrons from the core are dominant rather than the spallation neutrons produced by the proton beam. The DPAs by neutrons above 20 MeV based on the HTAPE results (dotted lines in Figs. 5.8.1-5.8.7) decrease with increasing k_{eff}, because the number of spallation neutrons declines owing to the fall off of the proton beam current. For MFT, the characteristics of DPA for PFT are held except for cells #9, #12, and #5 in the small k_{eff} region. The k_{eff} was changed by changing the core thickness, R. Since we assumed a constant power density, the total power changed when R was changed. Comparing the proton beam currents required to run MFT at k_{eff} = 0.46 (R = 10 cm), and k_{eff} = 0.71 (R = 20 cm), we see that the proton beam current at k_{eff} = 0.46 is lower than that at k_{eff} = 0.71 (see Table 5.2 (a) and (b)). Although k_{eff} is lower for MFT with R = 10 cm, the total power is also lower, and as a result, the necessary proton beam current is lower. This is why the DPAs at k_{eff} = 0.46 in cells #9, #12, and #5 where the spallation neutrons are dominant are small compared to those at k_{eff} = 0.71 for MFT.

Next, we discuss the DPA of slightly subcritical transmuter. From Figs. 5.8.1-5.8.7 and 5.9.1-5.9.6, the DPAs of lead target cell #5, which has the severest DPA in the system, are 162 dpa/yr at k_{eff} = 0.95, and 93 dpa/yr at k_{eff} = 0.99 for PFT, and 154 dpa/yr at k_{eff} = 0.95, and 82 dpa/yr at k_{eff} = 0.99 for MFT. Comparing DPA at k_{eff} = 0.99 to the one at k_{eff} = 0.95 gives about 57 % for PFT and about 53 % for MFT. These result indicate that using a very slightly subcritical transmuter greatly alleviates atomic displacement by a proton beam.

The energy deposition is the largest in the lead target cell #5, and the second largest in the beam window cell #9. Their energy depositions are more than 1000 watt/cm^3, and therefore, an effective cooling system should be considered. However, if a slightly subcritical transmuter is used, the energy deposition may be less because of a low proton beam current.

Hydrogen (H) and helium (He) production rates are also shown in Tables 5.1 and 5.2. The lead cell #5 and the beam window cell #9 have large H and He production rates, because they are directly effected by the proton beam. The He production rate is 20 % less than the H production rate in cell #5, while it is ~ 3 % in cell #9. The H and He production rates in cell #12 (the structural wall near the beam window) are not as large, unlike the large DPA in this cell. Generally, a higher proton beam current gives larger H and He production rates. However, this general rule is not obeyed in the core (cells #1, #2, and #3) for MFT. Fission neutrons and different core volumes for different Rs might change these characteristics. (The production rates were calculated by dividing the number of H and He produced in unit time by cell volume.) This analysis shows that the characteristics of radiation damage for PFT and MFT were the almost same. Cell #5 of the lead target, the beam window (cell #9), and cell #12 of the structural wall had large DPA. Cell #12 is a side wall near the beam window. This result indicates that in designing a proton accelerator-driven transmuter, the radiation damage of not only the beam window and the target should be carefully investigated but also the side wall near the beam window. For contributions to DPA by neutrons, those with energies below 20 MeV were dominant compared to those above 20 MeV.

A high proton beam current is necessary for a transmuter with a large degree of subcriticality, which means that the radiation damage caused by a proton accelerator becomes larger when a bigger subcritical transmuter is used.

The energy deposition, and the H and He production rates depended on the proton beam current. A higher beam current gave larger values, except in the core, because there, fission energy is mainly deposited, and the total fission energy mostly depends on the power density, not on the proton beam current. The beam window (cell #9) and the lead target near the beam window (cell #5) had large amounts of energy deposited and high production rates of H and He, although the He production rate was smaller than the former.

6. Conclusions

The damage to the structural materials of a proton-accelerator-based transmuter was investigated using Monte Carlo simulation codes LAHET, HMCNP, and HTAPE. Atomic displacement (DPA), H and He production rates, and energy deposition were evaluated. In calculating the DPA cross section, the TRANSX2 code was used. The tungsten target, the structural walls, and the core were divided into small cells to estimate the positional dependence of the radiation damage.

In this transmutor, Cell #31-35 of the tungsten target, the beam window (cell #41), and cell #43-48 of the structural wall have smaller DPA than the core regions. Since the fuel has tungsten material which has large neutron DPA cross section in energy range of 2 eV to 100 eV, and the neutron flux in the core is high, the reduction of proton current can not make the DPA small as the case of the MOX or particle fueled core.

The energy deposition, and the H and He production rates depended on the proton beam current. A higher beam current gave larger values, except in the core, because there, fission energy is mainly deposited. The beam window (cell #41) and the tungsten target near the beam window (cell #31-33) had large amounts of energy deposited and high production rates of H and He, although the He production rate was smaller than the former.

We calculated the radiation damage and heat deposition of these reactor in the case when it is run with 10 mA proton current, since the total thermal energy out put is 456 MW, and nominal power is 600 MW. Therefore, the proton current has to be increased to 13.15 mA, and the radiation damages are increased to this factor of 1.315. This becomes rather high radiation damage rate so that it requires the frequent replacement and results into the low plant factor. By choosing the smaller subcriticality, this difficulty can be avoided. Otherwise we need the search for materials which can stand for radiation damage or has the low DPA cross section.

The geometry, which is used in this calculation, is slightly different from the JAERI's recent design for transmutor, New design has wider tungsten target which is not go through the core, we are going to evaluate this new geometry in the next calculation.

Acknowledgment

We are grateful to Mr. A. Aronson for his help in calculations of this report. We would like to express our thanks to Drs. H.Takashita, H.Harada, T.Nishida, E.T. Cheng and R.E. MacFarlane for providing useful information. We wish to thank Dr. A.D. Woodhead for her editorial work. This work was supported by Japan Atomic Energy Research Institute, in Japan, and U.S. Department of Energy at Brookhaven National Laboratory under Contract No. DE-AC02-76CH00016.

References

1) H. TAKAHASHI and H. RIEF, "Concepts of Accelerator-Based Transmutation Systems," Proc. of the Specialists' Meeting on Accelerator-Based Transmutation, PSI Villigen, Switzerland, March 24-26, p. 2, Paul Scherrer Institute (1992).

2) T. TAKIZUKA, "Overview on Nuclear Design Problems of Accelerator-Based Transmutation Systems with Emphasis on Target Facilities and Their Interfaces with Accelerators," Proc. of the Specialists' Meeting on Accelerator-Based Transmutation, PSI Villigen, Switzerland, March 24-26, p.112, Paul Scherrer Institute (1992).

3) C. D. BOWMAN et al., "Nuclear Energy Generation and Waste Transmutation Using an Accelerator-Driven Intense Thermal Neutron Source," Nucl. Instr. and Meth. A320, 336 (1992).

4) H. TAKASHITA, H. HARADA, H. TAKAHASHI and A. ARONSON, "Transmutation of Long-Lived Radioactive Nuclides," Proc. of the International Conference and Technology Exposition on Future Nuclear System: Emerging Fuel Cycles and Waste Disposal Options GLOBAL '93, Seattle, Washington, Sep. 12-17, p. 797, American Nuclear Society (1993).

5) H. HARADA and H. TAKAHASHI, "Damage of Structural Material of a Nuclear-Waste Incinerator by Spallation Neutron," Int. Conf. on Application of Accelerators in Research and Industry, Univ. of North Texas, Nov. 2-5 (1992).

6) T. MUKAIYAMA, H. YOSHIDA and Y. GUNJI, "Minor Actinide Transmutation Using Minor Actinide Burner Reactors", Proc. Int. Conf. on Fast Reactors and Related Fuel Cycles FR91, Kyoto, Japan, Oct. 28 - Nov. 1, 19.6, Atomic Energy Society of Japan, Power Reactor and Nuclear Fuel Development Corporation, The Japan Atomic Power Company (1991).

7) J. F. BRIESMEISTER (Editor), "MCNP - A General Monte Carlo Code for Neutron and Photon Transport, Version 3A," LA-7396-M, Rev. 2, Los Alamos National Laboratory (1986).

8) R. E. PRAEL and H. LICHTENSTEIN, "User Guide to LCS: The LAHET Code System," LA-UR-89-3014, Los Alamos National Laboratory (1989).

9) R. E. MACFARLANE, "TRANSX2: A Code for Interfacing MATXS Cross-Section Libraries to Nuclear Transport Codes," LA-12312-MS, Los Alamos National Laboratory (1992).

10) YU. A. KOROVIN, A. YU. KONOBEYEV and V. N. SOSNIN, "BISERM, Neutron and Proton Data Library for Evaluation of Irradiation Effects in Structural Materials in the Energy Range up to 800 MeV," to be published.

11) A. Yu. KONOBEYEV, Yu. A. KOROVIN, and V. N. SOSNIN, "A Nuclear Data Library for Structural Material Radiation Damage Calculation at High Energies," Kerntechnik, 57, 188 (1992).

Table 2.1 Parameters for the design of tungsten target/MA metal fuel transmuter system

Core Composition		
Core region	Cross diameter	140 cm
(cylinder)	Cross inner radius	20 cm
	Height	140 cm
Target (1) region	(Beam in) (Multi-disk type)	
	Cross radius	20 cm
	Height	40 cm
Target (2) region	(Multi-disk type)	
	Cross radius	20 cm
	Height	100 cm
Up-Down reflector	Thickness	40 cm
R-direction reflector	Thickness	60 cm
Fuel	(Pin-bundle type)	
Composition	Np-15Pu-30Zr / AmCm-35Pu-10Y	
Bond Material		Na
Clad Material		ODS steel
Srug diameter		4 mm
Clad outer diameter		5.22 mm
Clad thickness		0.3 mm
Pin pitch		8.7 mm
Cluster shape		Hexagonal
Cool system		
Cooling material		Na
Input temperature		330 ℃
Maximum velocity		8 m/s

Table 2.2 Material composition in each region

Region	Target-1	Target-2	R-reflector	Z-reflector	Fuel
W-182	0.2642e-3	0.1058e-2			0.1953e-5
W-183	0.1437e-2	0.5750e-2			0.1062e-5
W-184	0.3084e-2	0.1235e-1			0.2280e-5
W-186	0.2873e-2	0.1151e-1			0.2124e-5
Na-23	0.2133e-1	0.9078e-2	0.7617e-2	0.1016e-2	0.1794e-1
Cr-nat			0.5569e-2	0.4774e-2	0.5946e-3
Mn-nat			0.3010e-3	0.2658e-3	0.2251e-4
Fe-nat			0.2059e-1	0.1765e-1	0.3906e-2
Ni-nat			0.3484e-2	0.2986e-2	0.2195e-4
Mo-nat			0.4438e-3	0.3804e-3	0.2739e-4
Pu-238					0.1717e-4
Pu-239					0.5351e-3
Pu-240					0.3880e-3
Pu-241					0.9167e-4
Pu-242					0.5000e-4
Np-237					0.1354e-2
Am-241					0.6476e-3
Am-243					0.2919e-3
Cm-243					0.7298e-6
Cm-244					0.1238e-3
Cm-245					0.6756e-5
C-nat					0.4076e-4
Si-nat					0.2660e-4
V-nat					0.1517e-4
Y-nat					0.5396e-3
Zr-nat					0.1919e-2

Table 4.1 Calculations of radiation damage of transmuter (Geometry 1)
$R^{a)}$ = 50 cm, k_{eff} = 0.966, $P^{b)}$ = 456 MW_{th}, $I_p^{c)}$ = 10 mA, E_p = 1 GeV

Cell #	Material	DPA[d] (dpa/yr)	W[e] (W/cm^3)	H[f] ($mol/cm^3/yr$)	He[g] ($mol/cm^3/yr$)
11	Fuel	149.1	1.6	4.2×10^{-6}	3.4×10^{-7}
	ODS	59.6	294.1[h]		
12	Fuel	125.0	0.5	1.4×10^{-6}	2.2×10^{-7}
	ODS	49.9	234.4[h]		
13	Fuel	87.2	0.2	5.0×10^{-7}	8.0×10^{-8}
	ODS	34.7	219.2[h]		
21	ODS	4.4	0.08	6.0×10^{-7}	3.3×10^{-8}
22		4.0	0.003	4.7×10^{-8}	6.2×10^{-9}
23		7.8	0.02	2.5×10^{-7}	1.3×10^{-8}
31	Tungsten	41.6	259.7	6.3×10^{-4}	1.5×10^{-4}
32		44.8	199.5	4.5×10^{-4}	1.0×10^{-4}
33		44.0	298.5	6.7×10^{-4}	8.0×10^{-5}
34		20.5	108.5	1.8×10^{-4}	1.6×10^{-5}
35		11.7	21.4	4.5×10^{-5}	0.0
36		4.0	0.4	2.1×10^{-6}	2.6×10^{-5}
40	Stainless	40.3	390.3	1.7×10^{-3}	8.3×10^{-5}
41		7.0	0.05	5.9×10^{-7}	0.0
42		23.4	1.3	8.5×10^{-6}	0.0
43		40.2	18.3	8.1×10^{-5}	3.5×10^{-6}
44		49.9	35.4	1.6×10^{-4}	7.0×10^{-6}
45		47.1	29.3	1.6×10^{-4}	1.1×10^{-5}
46		30.5	13.9	5.3×10^{-5}	0.0
47		20.8	5.3	4.0×10^{-5}	2.4×10^{-6}
48		6.4	0.4	1.8×10^{-6}	0.0

a) Core thickness in the radial direction
b) Total thermal power
c) Proton beam current required to operate the transmuter continuously
d) Atomic displacement
e) Energy deposition
f) H production rate
g) He production rate
h) Energy generation by fission in core

Table 5.1 Calculations of radiation damage of particle fuel transmuter (PFT)
(a) R[a] = 10 cm, k_{eff} = 0.631, P[b] = 85.7 MW_{th}, I_p[c] = 24.4 mA

Cell #	Material	DPA[d] (dpa/yr)	W[e] (W/cm^3)	H[f] ($mol/cm^3/yr$)	He[g] ($mol/cm^3/yr$)
1	Fuel	56.5	689.3	4.8×10^{-5}	1.1×10^{-5}
2	Fuel	48.6	616.1	2.8×10^{-5}	5.9×10^{-6}
3	Fuel	41.6	582.0	2.5×10^{-5}	4.9×10^{-6}
4	Stainless	3.7	0.3	3.2×10^{-6}	1.4×10^{-7}
5	Lead	348.1	1924.2	4.5×10^{-3}	9.3×10^{-4}
6	Lead	97.7	353.7	5.1×10^{-4}	6.5×10^{-5}
7	Lead	16.1	3.4	1.9×10^{-5}	5.3×10^{-6}
8	Lead	2.8	4.8×10^{-2}	$<10^{-6}$	$<10^{-6}$
9	Stainless	205.5	1474.0	7.1×10^{-3}	2.4×10^{-4}
10	Stainless	11.8	0.3	2.4×10^{-6}	2.4×10^{-6}
11	Stainless	59.4	4.7	4.4×10^{-5}	2.4×10^{-6}
12	Stainless	173.5	53.9	3.8×10^{-4}	2.1×10^{-5}
13	Stainless	76.0	49.0	2.0×10^{-4}	1.4×10^{-5}
14	Stainless	16.8	1.5	1.2×10^{-5}	$<10^{-7}$
15	Stainless	3.2	$<10^{-6}$	$<10^{-6}$	$<10^{-7}$

a) Core thickness in the radial direction
b) Total thermal power
c) Proton beam current required to operate the transmuter continuously
d) Atomic displacement
e) Energy deposition
f) H production rate
g) He production rate

Table 5.1 (Continued)
(b) R[a] = 20 cm, k_{eff} = 0.882, P[b] = 228.6 MW_{th}, I_p[c] = 13.7 mA

Cell #	Material	DPA[d] (dpa/yr)	W[e] (W/cm^3)	H[f] ($mol/cm^3/yr$)	He[g] ($mol/cm^3/yr$)
1	Fuel	66.6	893.9	2.1×10^{-5}	4.9×10^{-6}
2	Fuel	57.6	781.8	1.1×10^{-5}	2.4×10^{-6}
3	Fuel	45.4	608.7	6.1×10^{-6}	1.7×10^{-6}
4	Stainless	5.1	0.1	1.3×10^{-6}	6.6×10^{-8}
5	Lead	241.9	1076.8	2.5×10^{-3}	5.2×10^{-4}
6	Lead	99.0	198.1	2.9×10^{-4}	3.6×10^{-5}
7	Lead	30.7	1.8	8.9×10^{-6}	3.0×10^{-6}
8	Lead	6.1	2.7×10^{-2}	$<10^{-6}$	$<10^{-8}$
9	Stainless	160.2	822.5	3.9×10^{-3}	1.3×10^{-4}
10	Stainless	16.4	5.7×10^{-2}	$<10^{-6}$	$<10^{-8}$
11	Stainless	66.4	2.7	2.1×10^{-5}	1.3×10^{-6}
12	Stainless	151.2	29.8	2.2×10^{-4}	9.2×10^{-6}
13	Stainless	88.3	27.3	1.1×10^{-4}	9.2×10^{-6}
14	Stainless	36.3	0.8	7.9×10^{-6}	$<10^{-8}$
15	Stainless	7.6	8.0×10^{-3}	$<10^{-6}$	$<10^{-8}$

a) Core thickness in the radial direction
b) Total thermal power
c) Proton beam current required to operate the transmuter continuously
d) Atomic displacement
e) Energy deposition
f) H production rate
g) He production rate

Table 5.2 Calculations of radiation damage of MOX fuel transmuter (MFT)
(a) $R^{a)}$ = 10 cm, k_{eff} = 0.461, $P^{b)}$ = 60 MW_{th}, $I_p^{c)}$ = 22.5 mA

Cell #	Material	DPA[d] (dpa/yr)	W[e] (W/cm^3)	H[f] ($mol/cm^3/yr$)	He[g] ($mol/cm^3/yr$)
1	Fuel	65.0	419.5	5.3×10^{-5}	9.3×10^{-6}
2	Fuel	53.7	391.8	3.5×10^{-5}	8.4×10^{-6}
3	Fuel	44.1	409.7	2.9×10^{-5}	7.3×10^{-6}
4	Stainless	2.8	0.2	2.6×10^{-6}	1.2×10^{-7}
5	Lead	321.6	1768.5	4.1×10^{-3}	8.5×10^{-4}
6	Lead	89.2	324.9	4.7×10^{-4}	6.0×10^{-5}
7	Lead	10.6	3.4	1.8×10^{-5}	4.9×10^{-6}
8	Lead	1.7	4.4×10^{-2}	$<10^{-6}$	$<10^{-7}$
9	Stainless	182.0	1353.4	6.5×10^{-3}	2.2×10^{-4}
10	Stainless	7.8	0.3	4.3×10^{-6}	$<10^{-7}$
11	Stainless	49.5	4.2	4.1×10^{-5}	$<10^{-7}$
12	Stainless	162.3	47.4	3.5×10^{-4}	1.1×10^{-5}
13	Stainless	71.4	45.4	1.7×10^{-4}	1.5×10^{-5}
14	Stainless	14.3	1.0	1.9×10^{-5}	$<10^{-7}$
15	Stainless	2.3	$<10^{-6}$	$<10^{-6}$	$<10^{-7}$

a) Core thickness in the radial direction
b) Total thermal power
c) Proton beam current required to operate the transmuter continuously
d) Atomic displacement
e) Energy deposition
f) H production rate
g) He production rate

Table 5.2 (Continued)

(a) $R^{a)} = 20$ cm, $k_{eff} = 0.711$, $P^{b)} = 160\ MW_{th}$, $I_p^{c)} = 24.0$ mA

Cell #	Material	DPA[d] (dpa/yr)	W[e] (W/cm^3)	H[f] ($mol/cm^3/yr$)	He[g] ($mol/cm^3/yr$)
1	Fuel	87.4	592.3	4.6×10^{-5}	9.4×10^{-6}
2	Fuel	67.2	450.7	2.2×10^{-5}	5.8×10^{-6}
3	Fuel	49.2	449.8	1.3×10^{-5}	3.1×10^{-6}
4	Stainless	4.0	0.2	2.0×10^{-6}	1.1×10^{-7}
5	Lead	364.1	1886.9	4.4×10^{-3}	9.1×10^{-4}
6	Lead	117.3	347.3	5.0×10^{-4}	6.5×10^{-5}
7	Lead	24.5	3.7	2.1×10^{-5}	5.2×10^{-6}
8	Lead	6.0	4.7×10^{-2}	$<10^{-6}$	$<10^{-7}$
9	Stainless	221.8	1435.9	6.8×10^{-3}	2.3×10^{-4}
10	Stainless	15.4	0.2	2.3×10^{-6}	$<10^{-7}$
11	Stainless	73.3	4.9	5.0×10^{-5}	2.3×10^{-6}
12	Stainless	197.4	47.0	3.6×10^{-4}	9.2×10^{-6}
13	Stainless	95.8	48.5	1.8×10^{-4}	1.4×10^{-5}
14	Stainless	30.0	0.6	9.2×10^{-6}	$<10^{-7}$
15	Stainless	6.0	5.7×10^{-2}	2.3×10^{-6}	$<10^{-7}$

a) Core thickness in the radial direction
b) Total thermal power
c) Proton beam current required to operate the transmuter continuously
d) Atomic displacement
e) Energy deposition
f) H production rate
g) He production rate

Table 5.2 (Continued)

(a) $R^{a)} = 30$ cm, $k_{eff} = 0.858$, $P^{b)} = 300$ MW_{th}, $I_p^{c)} = 16.8$ mA

Cell #	Material	DPA[d] (dpa/yr)	W[e] (W/cm^3)	H[f] ($mol/cm^3/yr$)	He[g] ($mol/cm^3/yr$)
1	Fuel	88.5	600.1	2.7×10^{-5}	5.3×10^{-6}
2	Fuel	71.1	503.2	8.8×10^{-6}	3.3×10^{-6}
3	Fuel	51.4	481.6	4.2×10^{-5}	1.2×10^{-6}
4	Stainless	5.3	0.1	1.1×10^{-6}	6.1×10^{-8}
5	Lead	273.1	1322.1	3.1×10^{-3}	6.3×10^{-4}
6	Lead	98.1	242.7	3.5×10^{-4}	4.5×10^{-5}
7	Lead	33.6	2.4	1.3×10^{-5}	3.6×10^{-6}
8	Lead	6.6	6.0×10^{-2}	$<10^{-6}$	$<10^{-8}$
9	Stainless	160.7	1003.8	4.9×10^{-3}	1.6×10^{-4}
10	Stainless	15.8	0.1	1.6×10^{-6}	$<10^{-8}$
11	Stainless	67.8	3.4	2.9×10^{-5}	3.2×10^{-6}
12	Stainless	167.7	34.4	2.7×10^{-4}	9.7×10^{-6}
13	Stainless	96.8	33.1	1.2×10^{-4}	9.7×10^{-6}
14	Stainless	39.7	0.4	6.5×10^{-6}	$<10^{-8}$
15	Stainless	8.7	$<10^{-6}$	$<10^{-6}$	$<10^{-8}$

a) Core thickness in the radial direction
b) Total thermal power
c) Proton beam current required to operate the transmuter continuously
d) Atomic displacement
e) Energy deposition
f) H production rate
g) He production rate

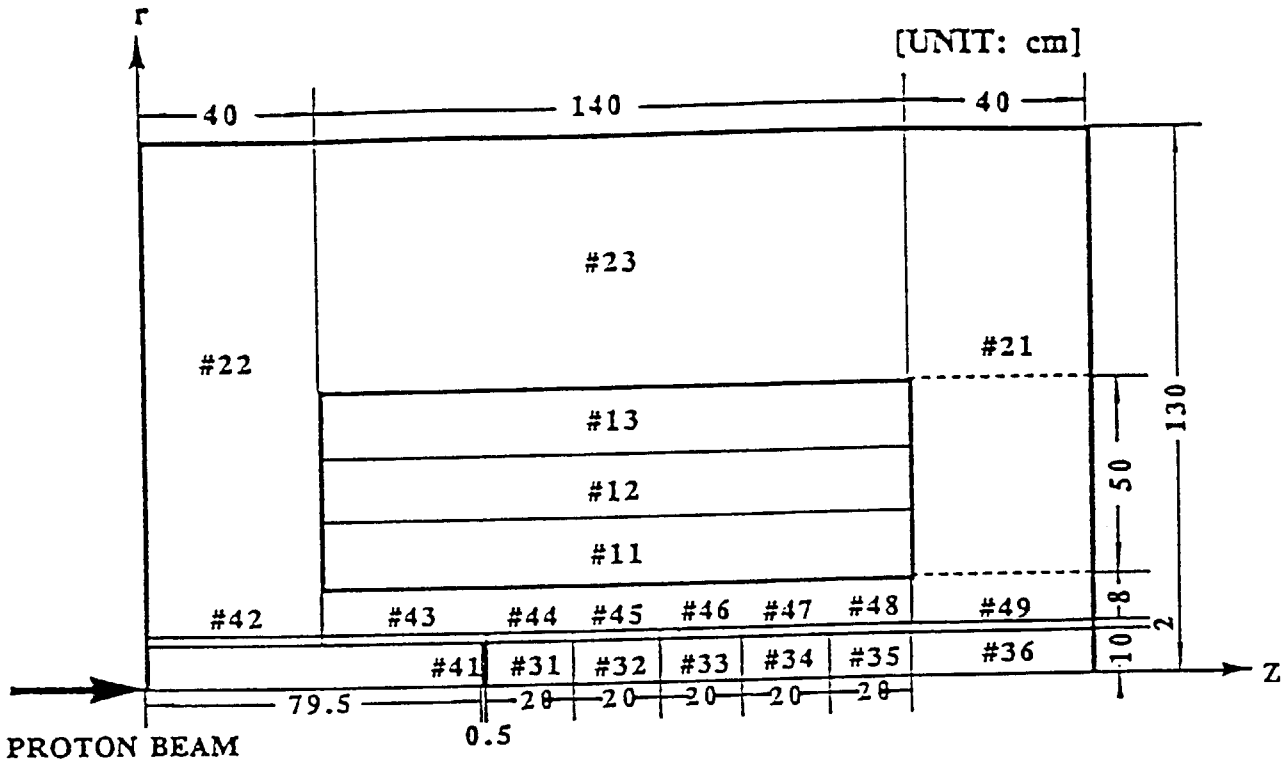

CORE: #11 - #13
REFLECTOR: #21 - #23
TUNGSTEN TARGET: #31 - #36
BEAM WINDOW: #41
STRUCTURAL WALL: #42 - #49

GEOMETRY 1

Fig 2.1 Cross sectional view of the calculational geometry

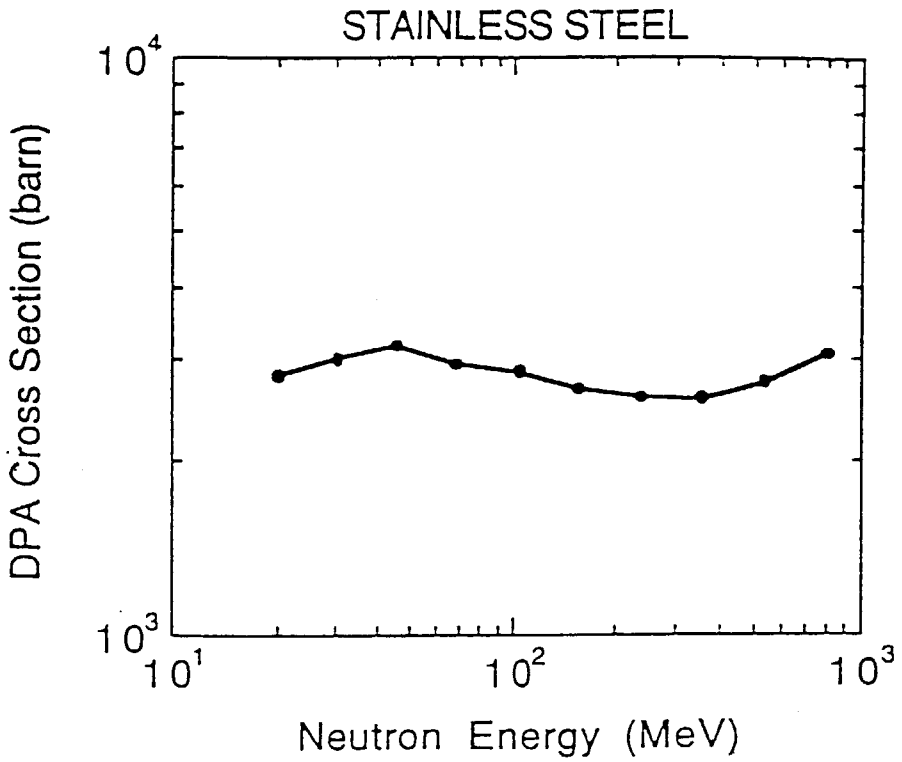

Fig.3.1.1 DPA cross section of stainless steel for neutron energies from 20 to 800 MeV

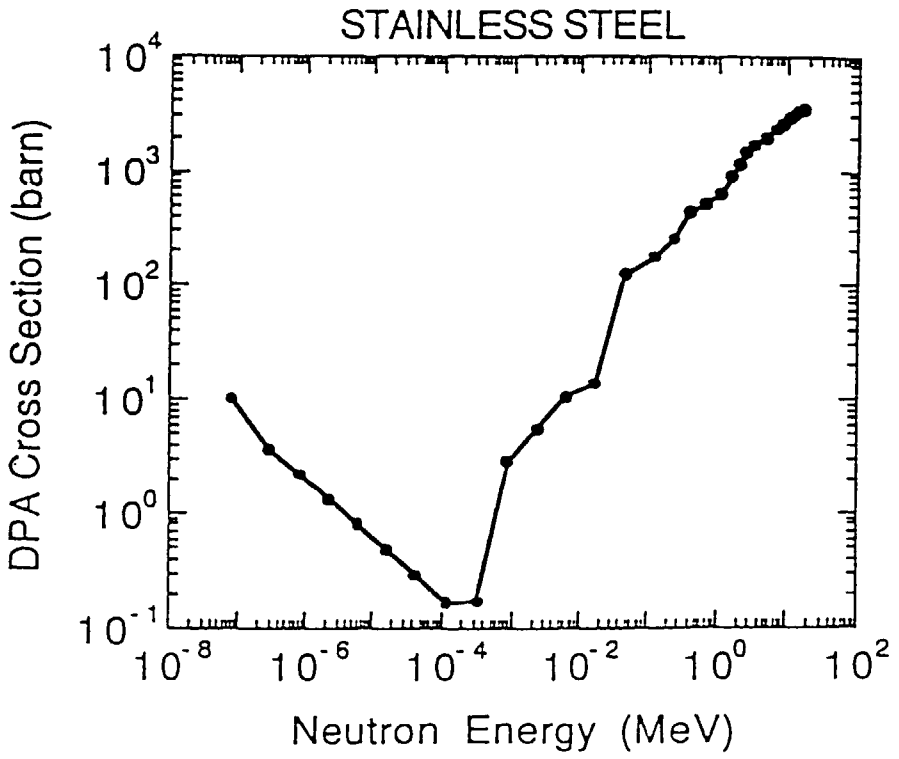

Fig.3.1.2 DPA cross section of stainless steel for neutron energies from 10^{-7} to 20 MeV

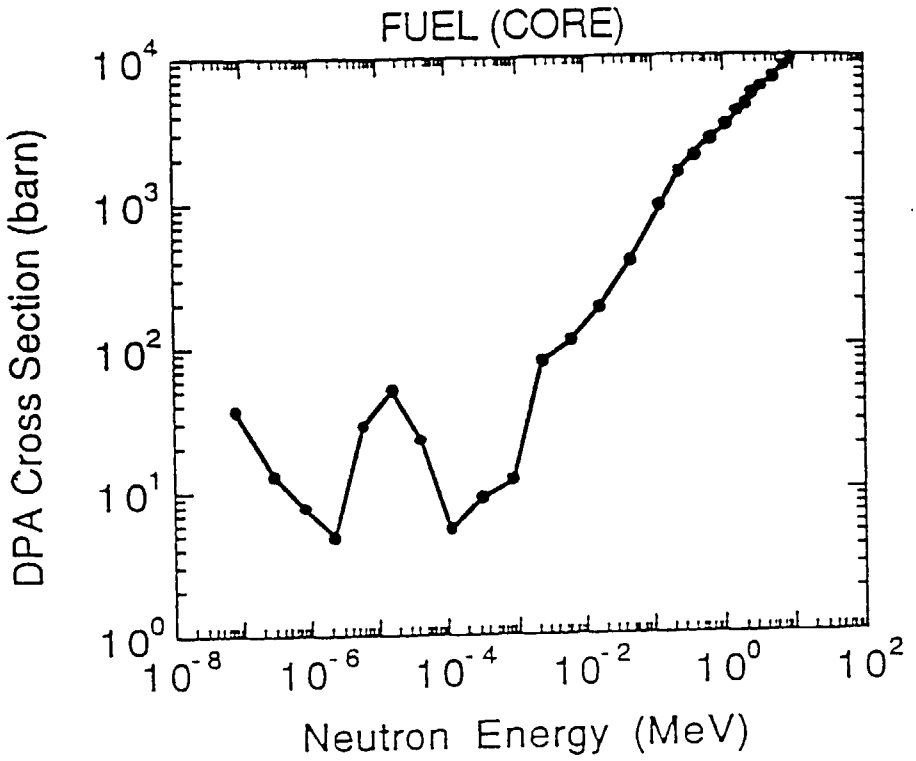

Fig.3.1.3 DPA cross section of fuel for neutron energies from 10^{-7} to 20 MeV

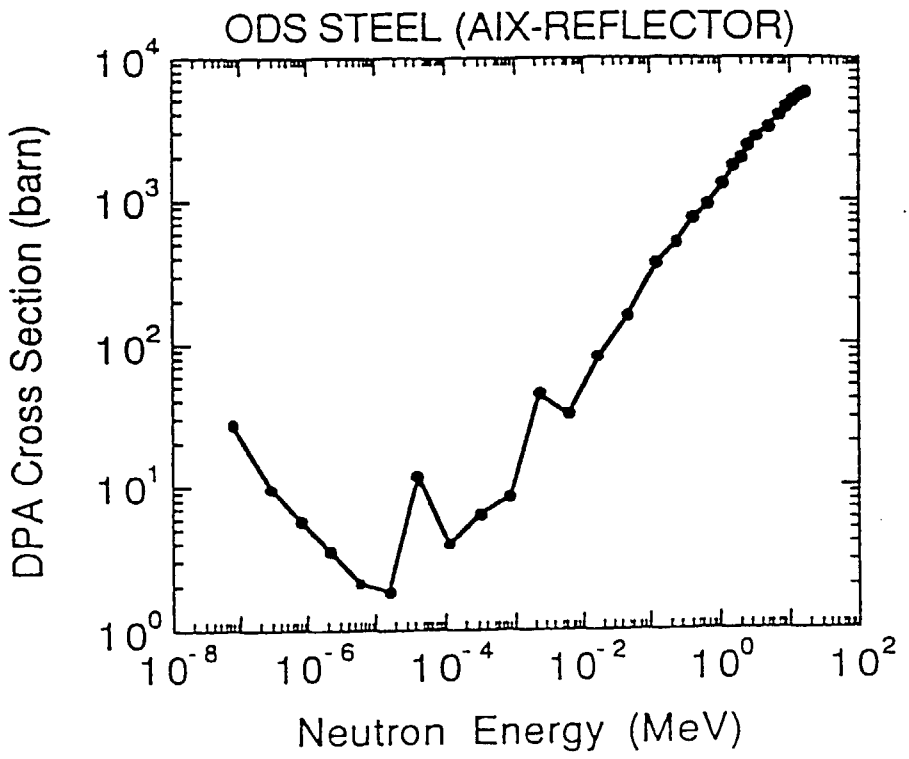

Fig.3.1.4 DPA cross section of axial reflector for neutron energies from 10^{-7} to 20 MeV

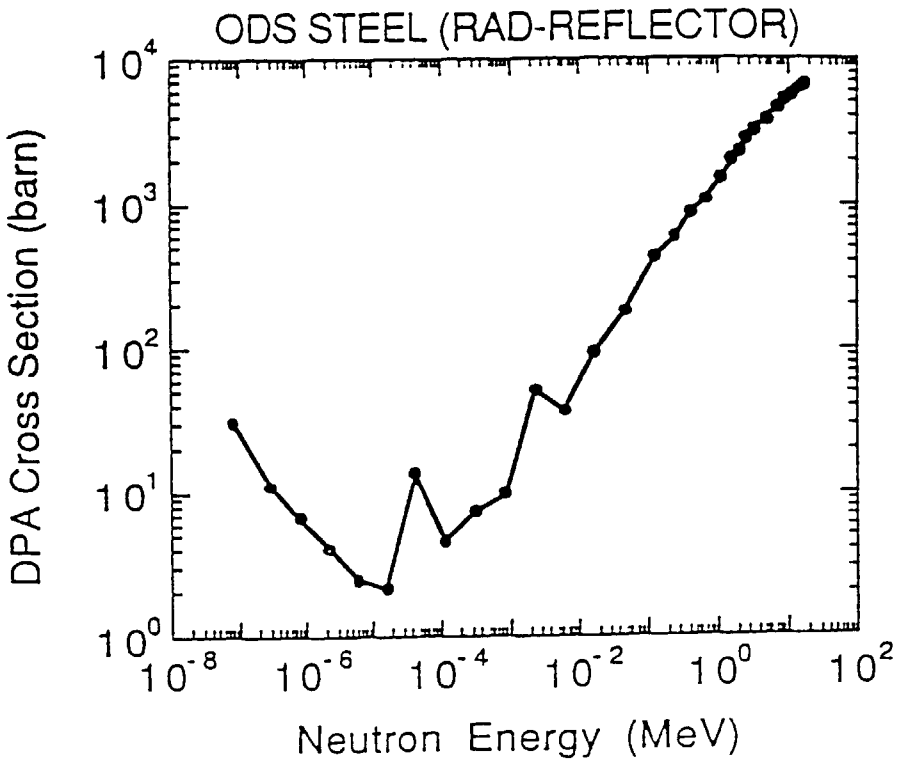

Fig.3.1.5 DPA cross section of radial reflector for neutron energies from 10^{-7} to 20 MeV

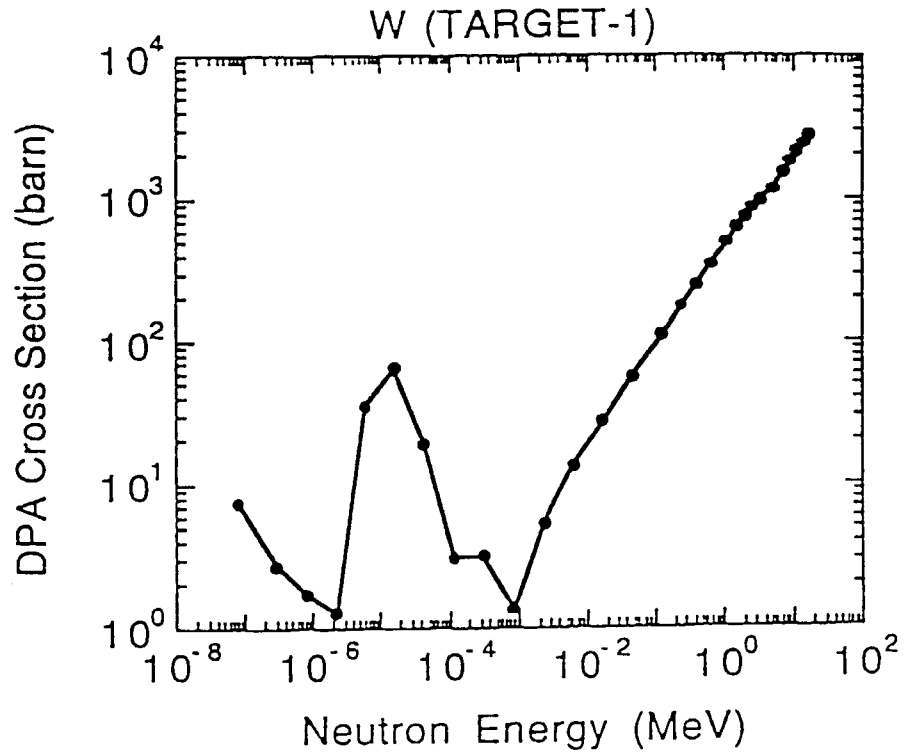

Fig.3.1.6 DPA cross section of target-1 for neutron energies from 10^{-7} to 20 MeV

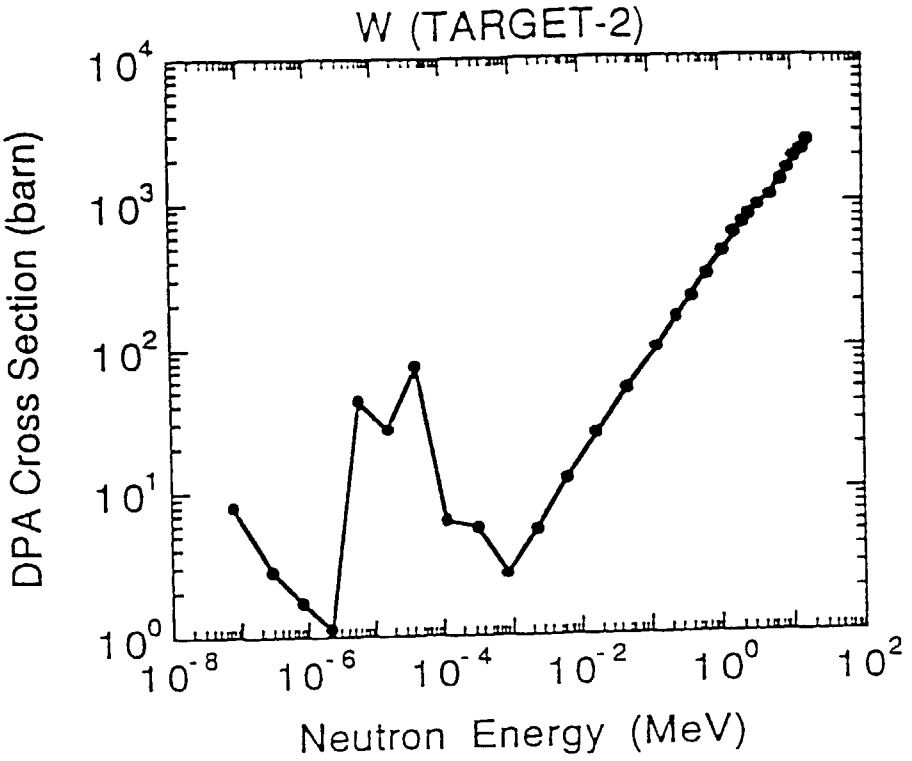

Fig.3.1.7 DPA cross section of target-2 for neutron energies from 10^{-7} to 20 MeV

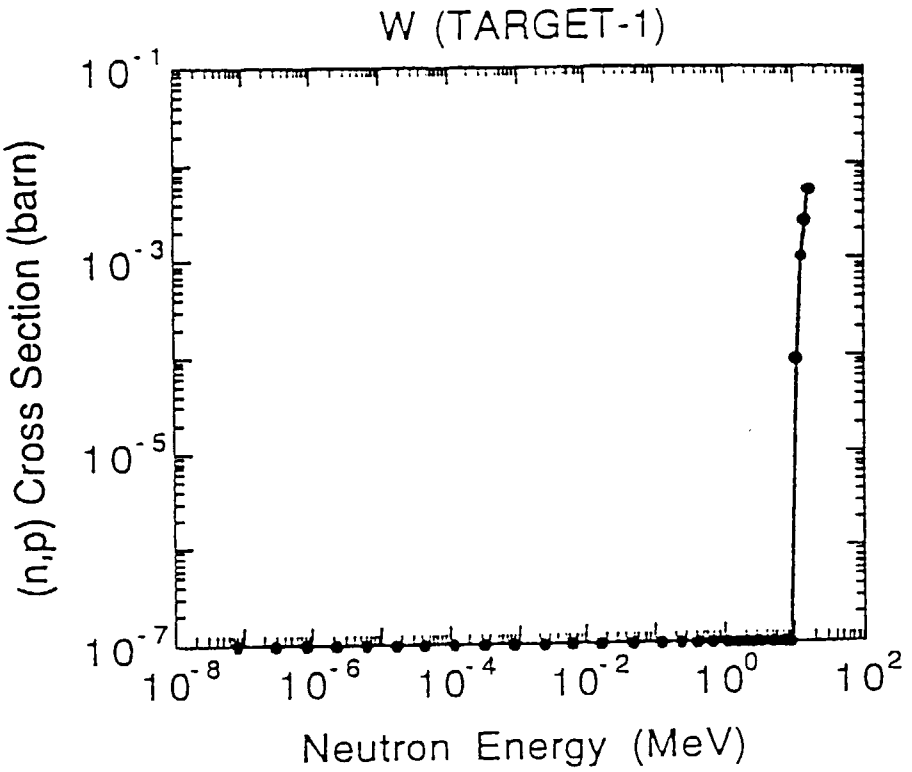

Fig.3.2.1 (n, p) cross section for target-1

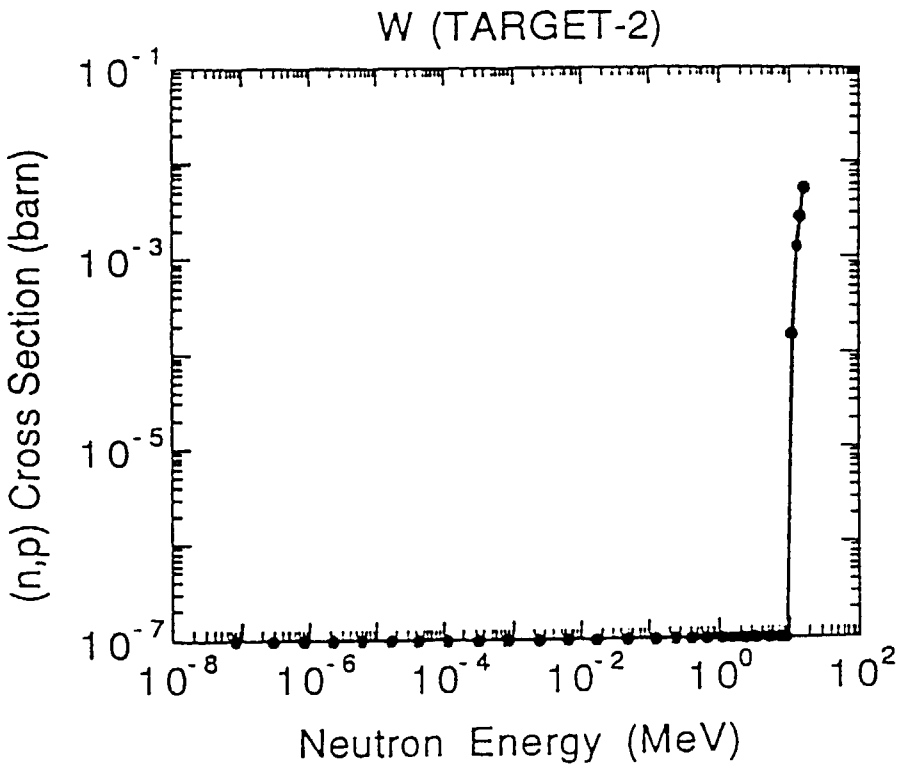

Fig.3.2.2 (n, p) cross section for target-2

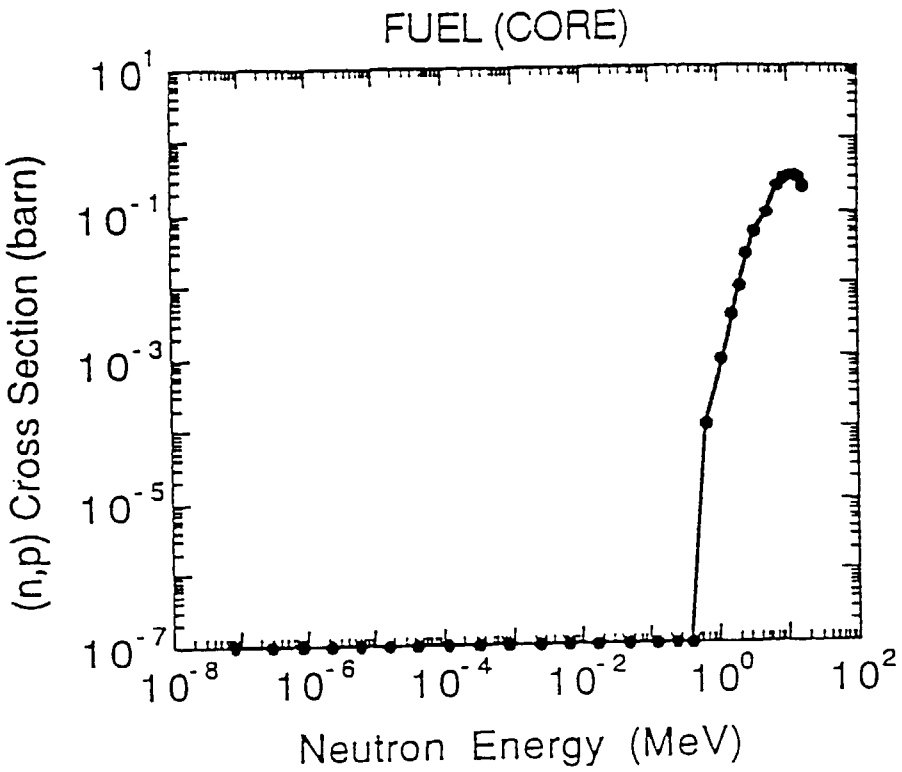

Fig.3.2.3 (n, p) cross section for fuel

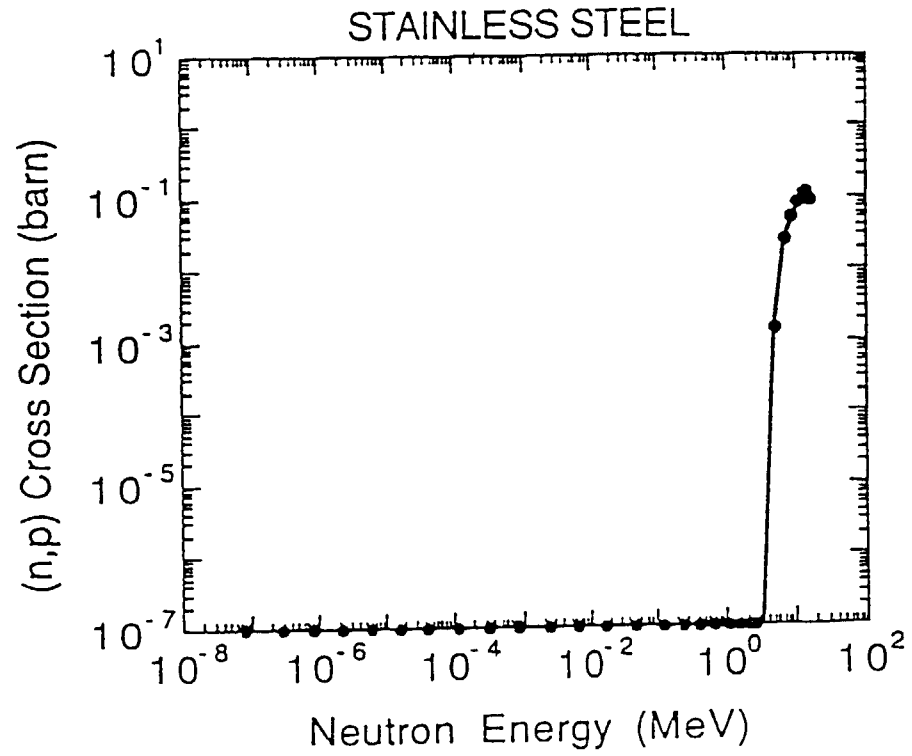

Fig.3.2.4 (n, p) cross section for stainless steel

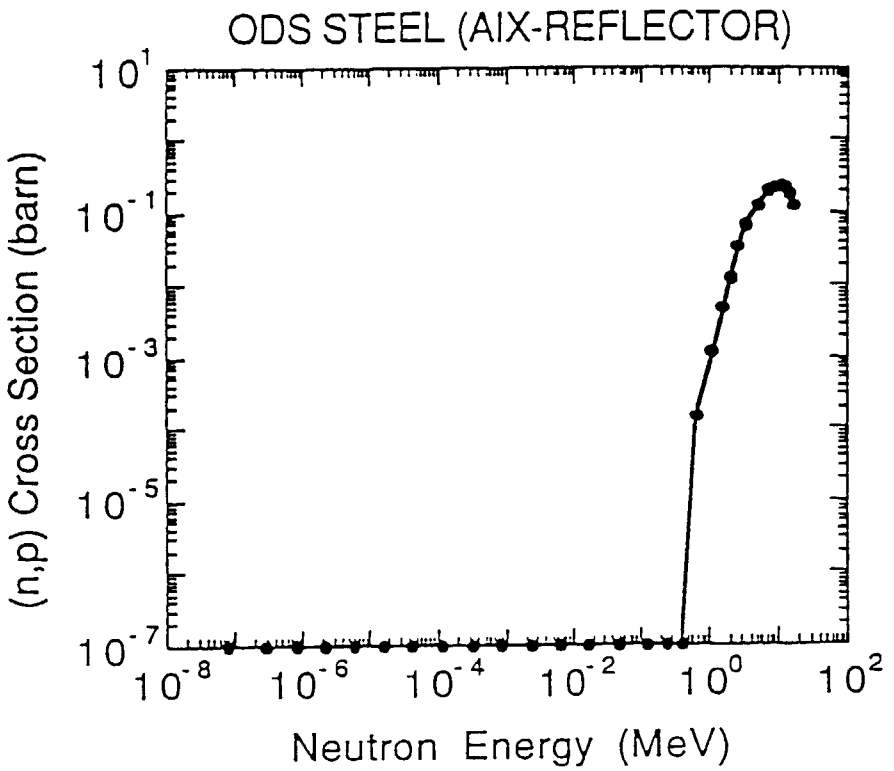

Fig.3.2.5 (n, p) cross section for axial reflector

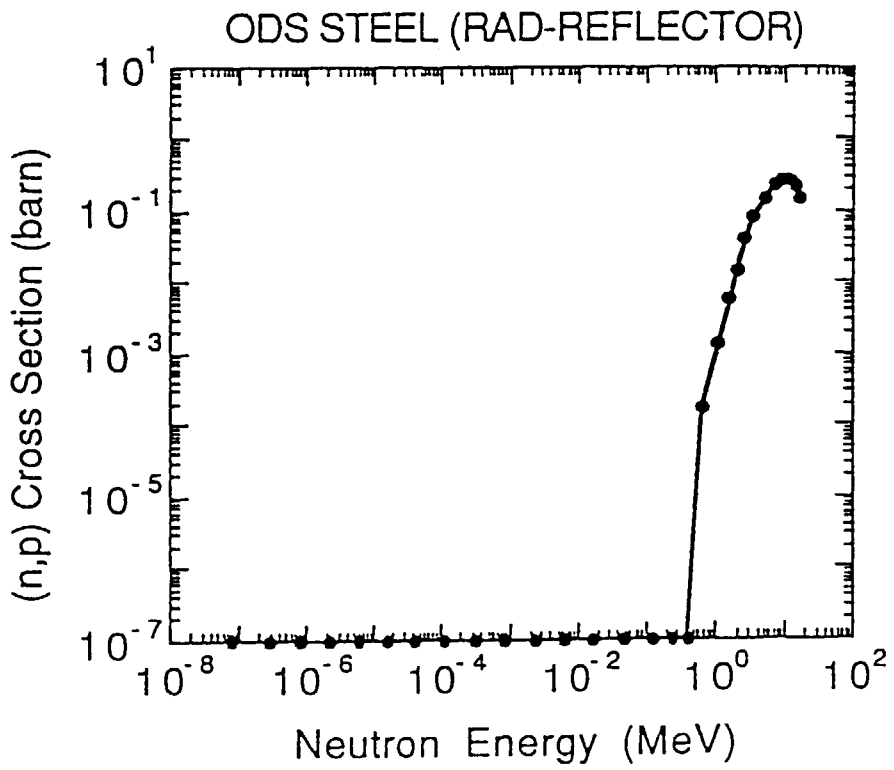

Fig.3.2.6 (n, p) cross section for radial reflector

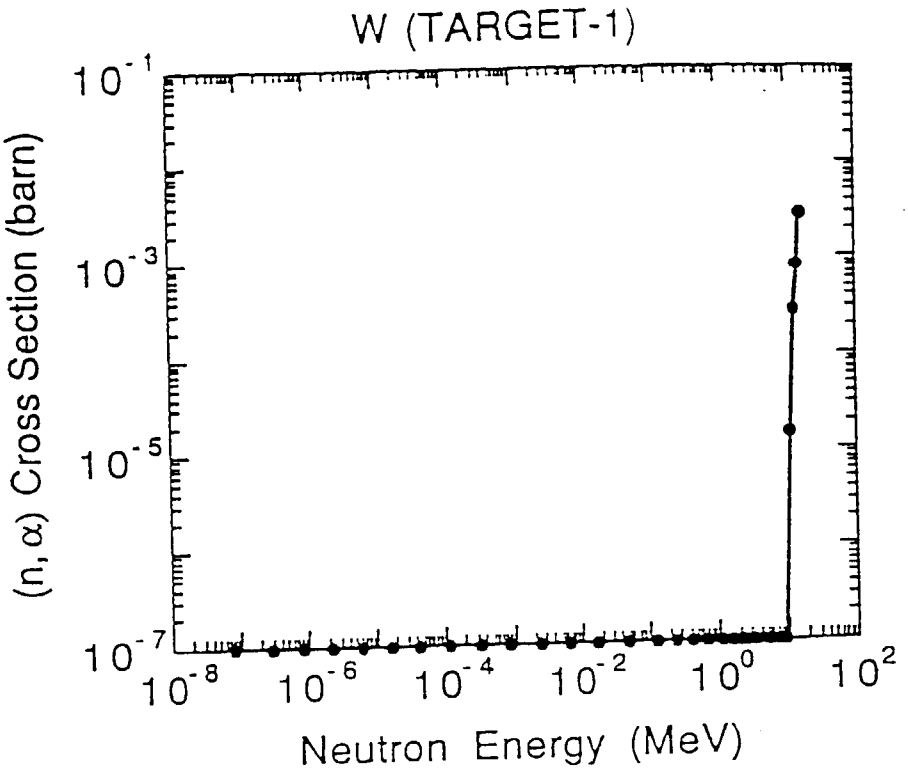

Fig.3.3.1 (n, α) cross section for target-1

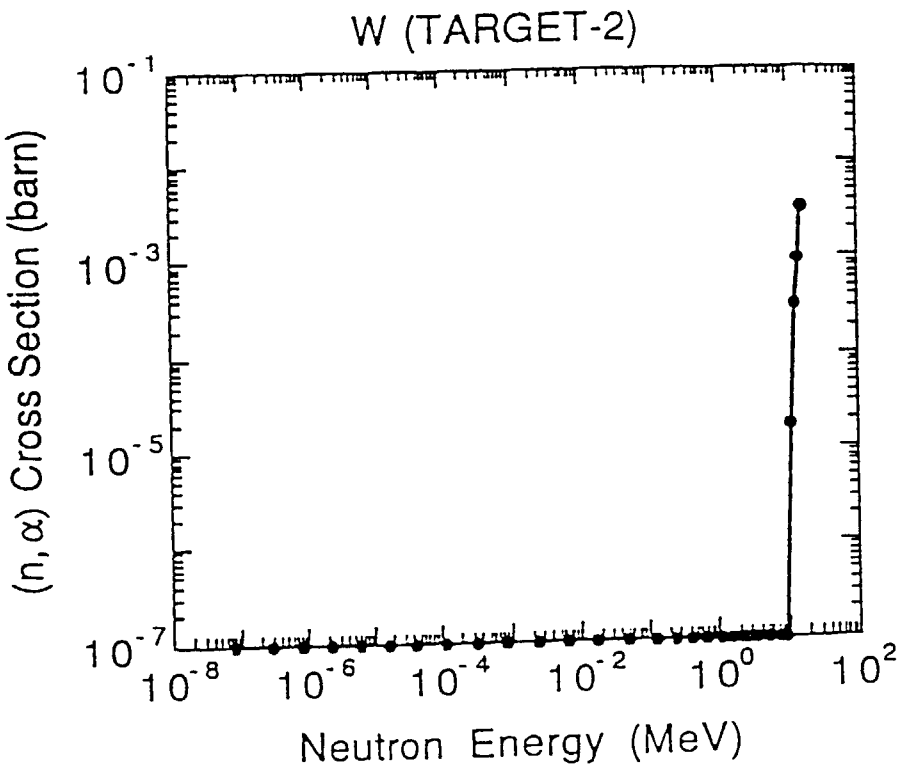

Fig.3.3.2 (n, α) cross section for target-2

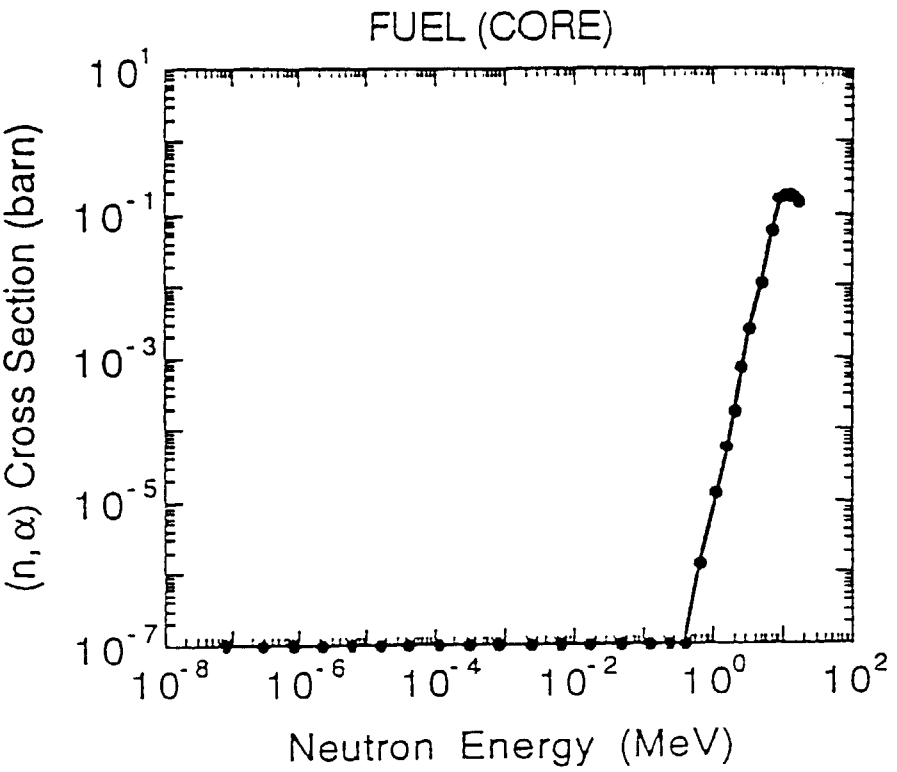

Fig.3.3.3 (n, α) cross section for fuel

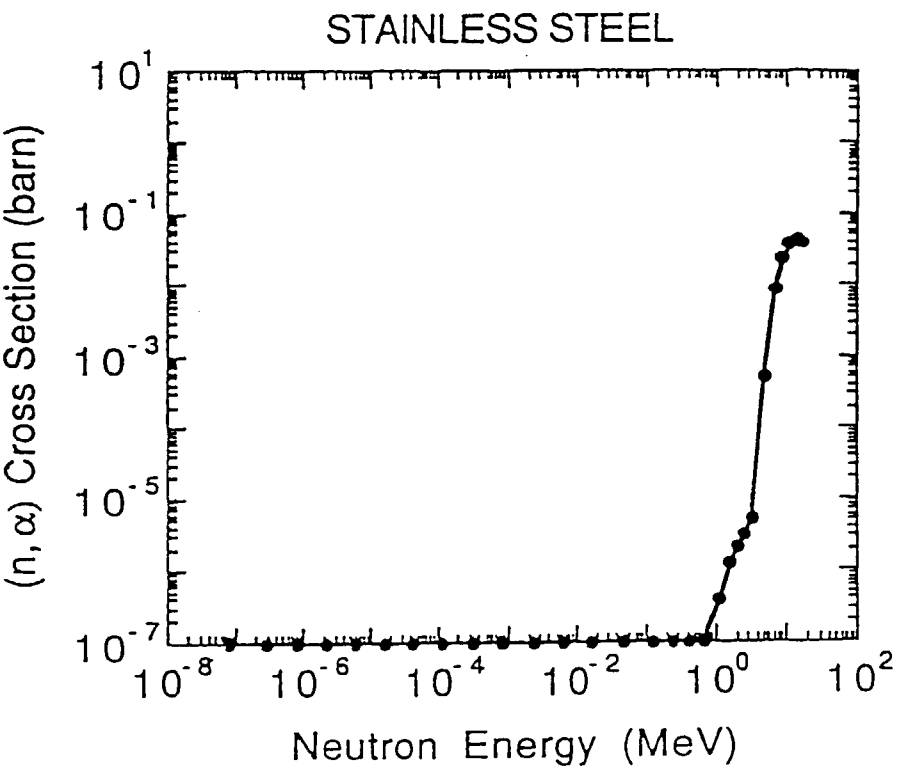

Fig.3.3.4 (n, α) cross section for stainless steel

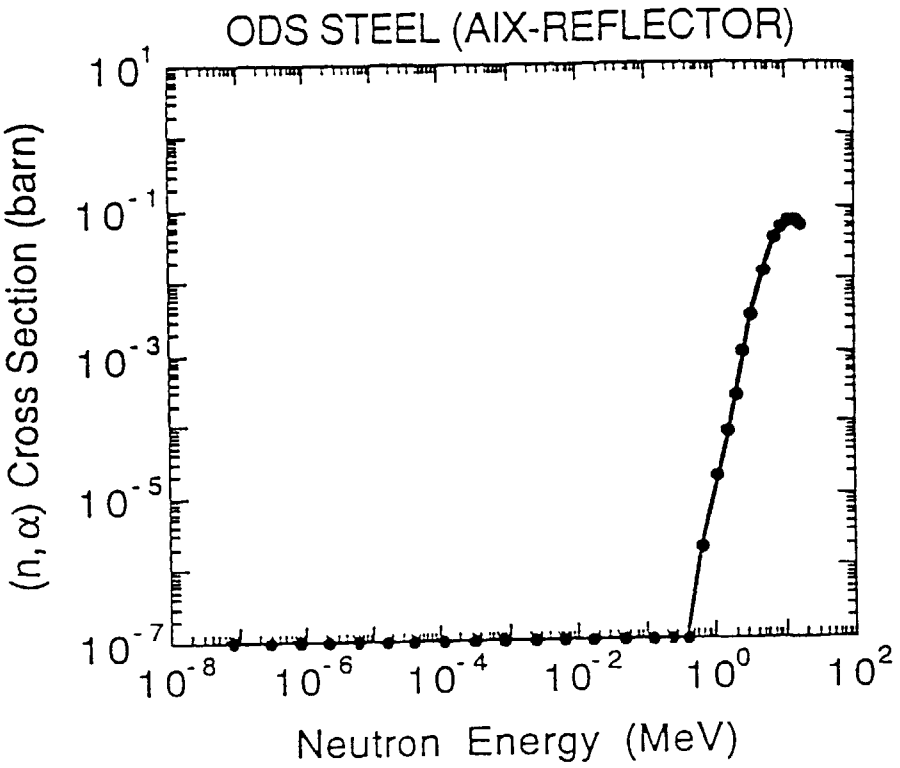

Fig.3.3.5 (n, α) cross section for axial reflector

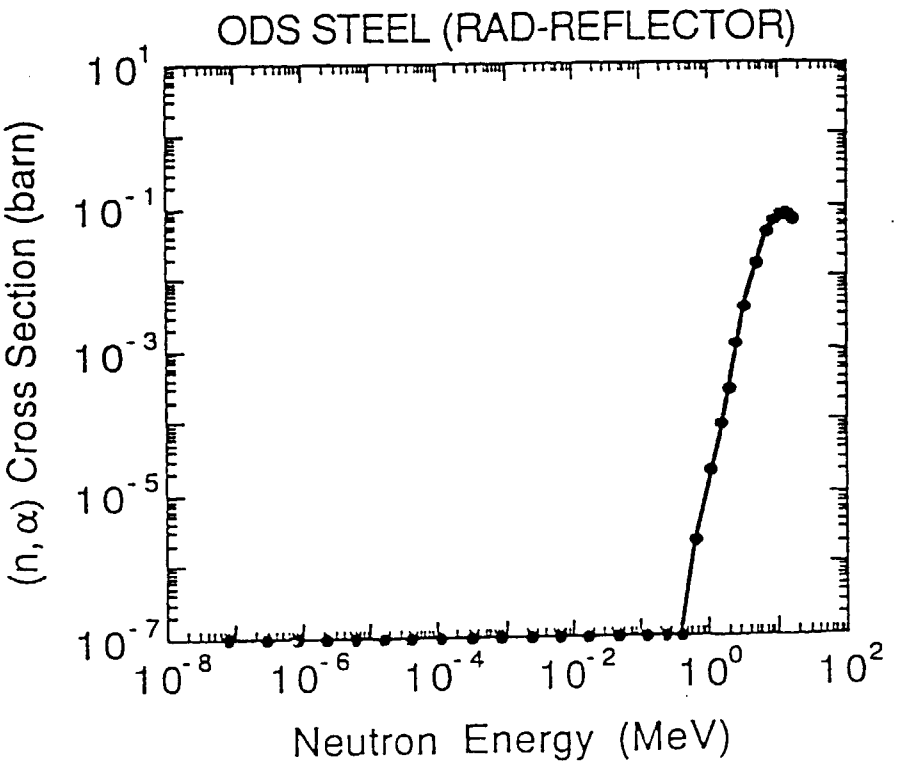

Fig.3.3.6 (n, α) cross section for radial reflector

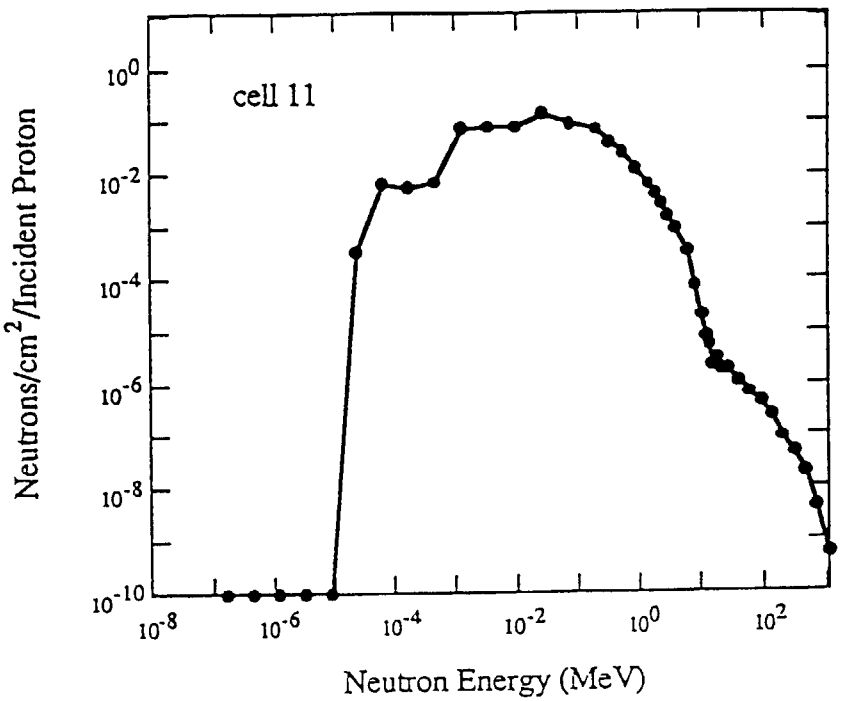

Fig.4.1.1 Neutron spectra in cell #11

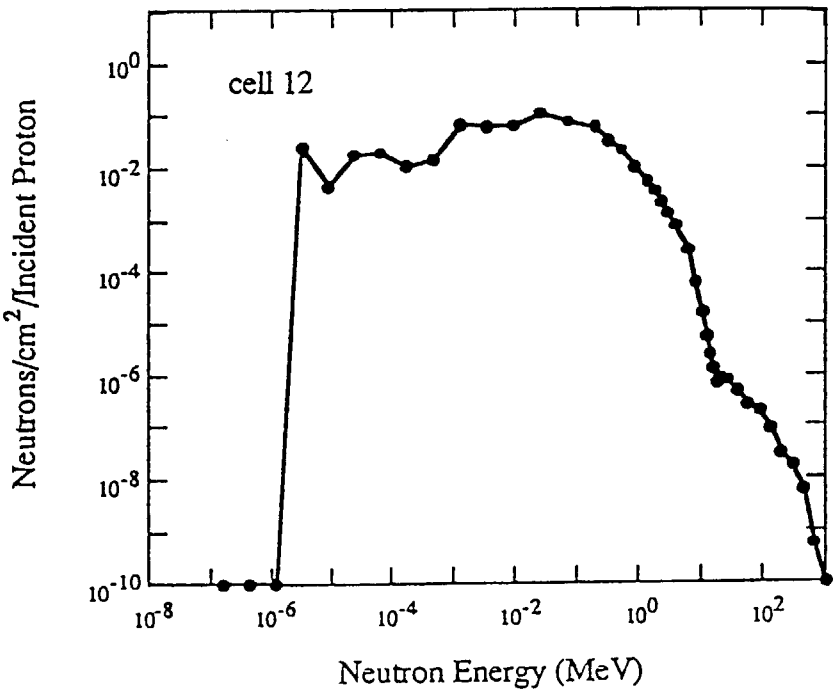

Fig.4.1.2 Neutron spectra in cell #12

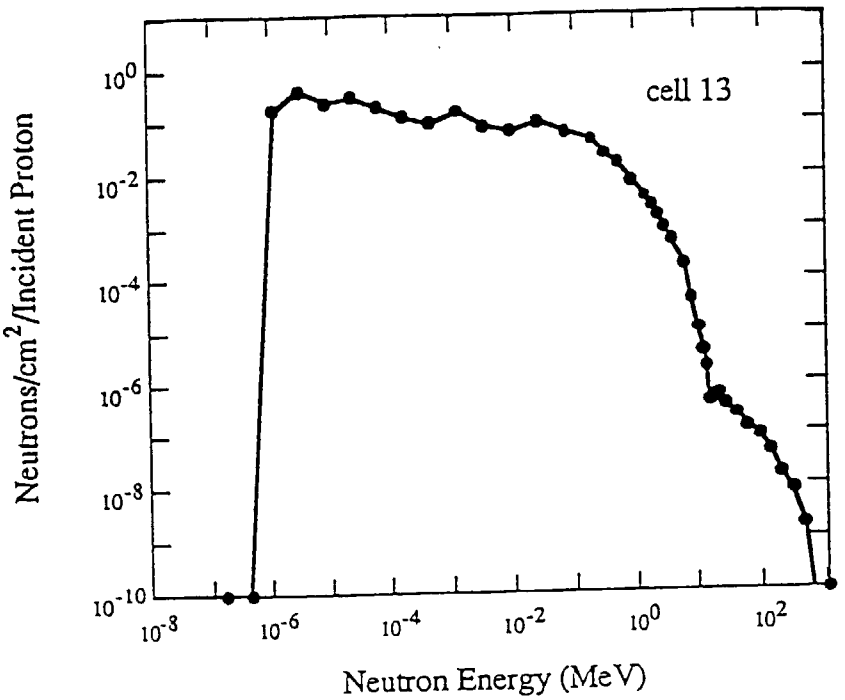

Fig.4.1.3 Neutron spectra in cell #13

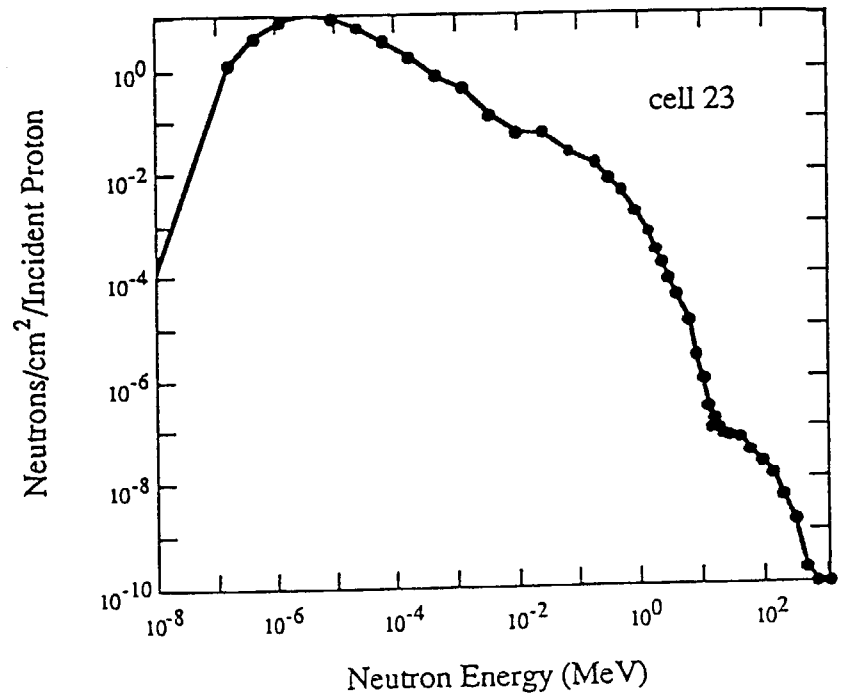

Fig.4.1.4 Neutron spectra in cell #23

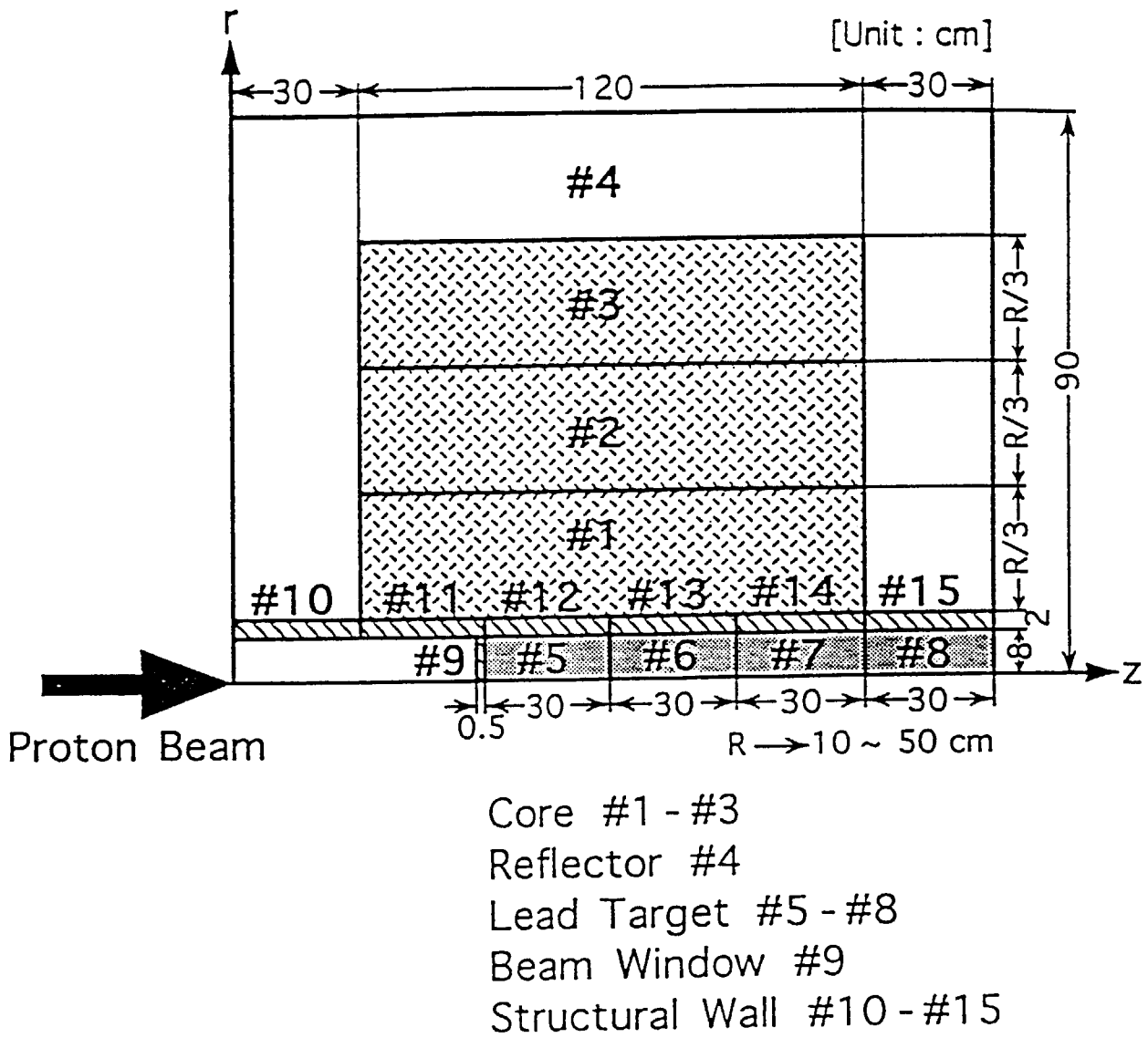

Fig.5.1 Cross sectional view of the calculational geometry (MFT and PFT)

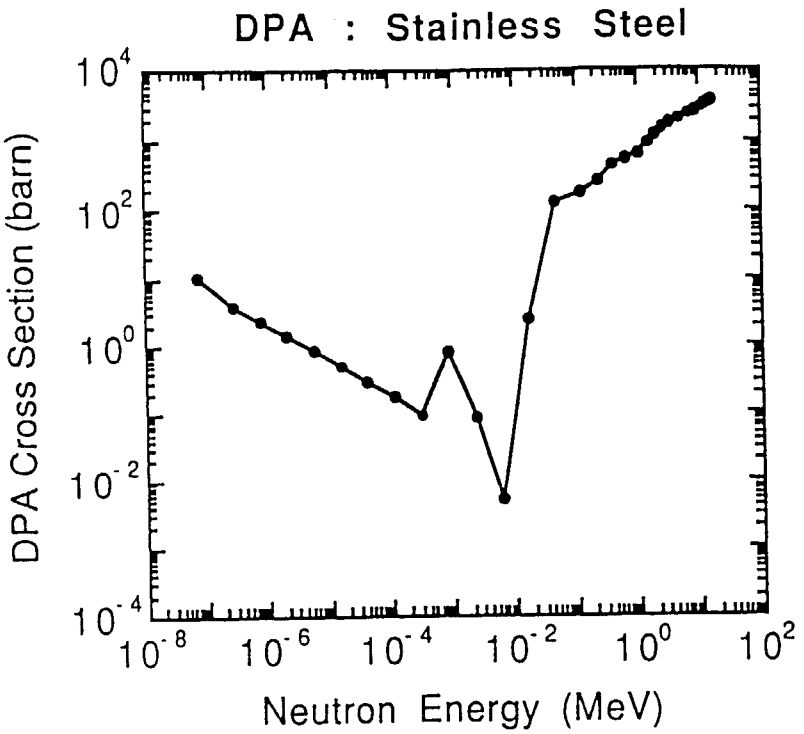

Fig.5.2.1 DPA cross section of stainless steel

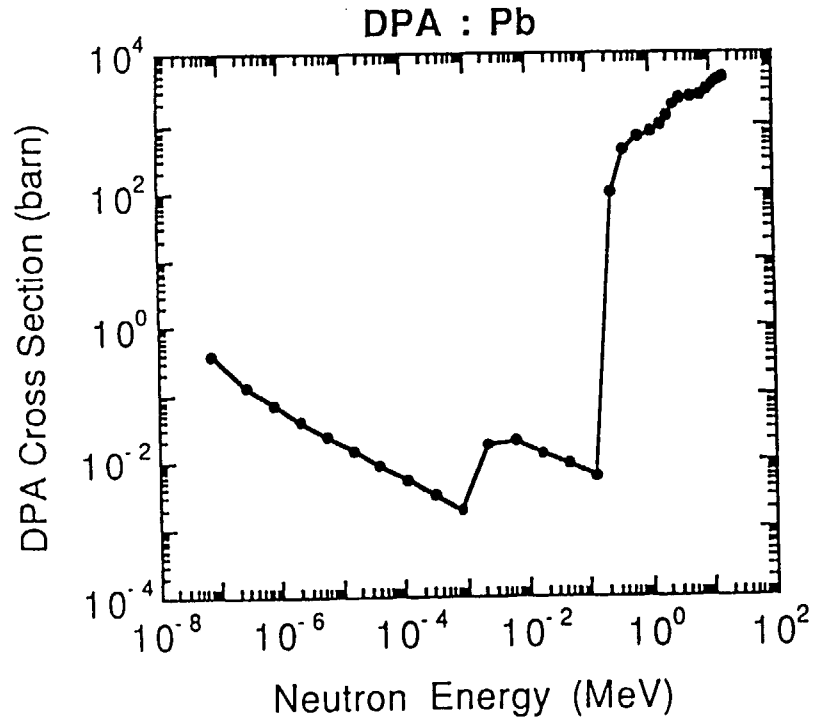

Fig.5.2.2 DPA cross section of lead

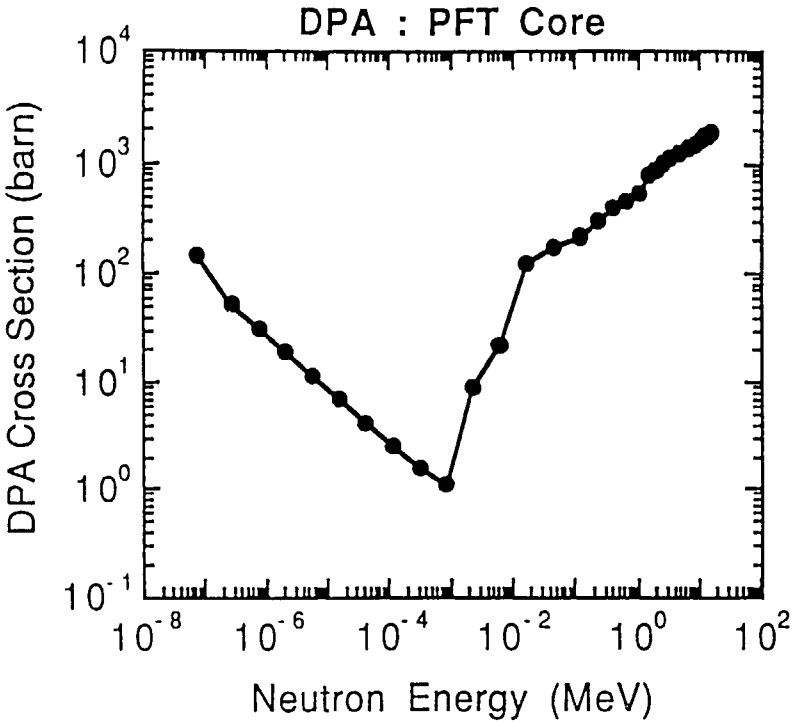

Fig.5.2.3 DPA cross section of PFT core

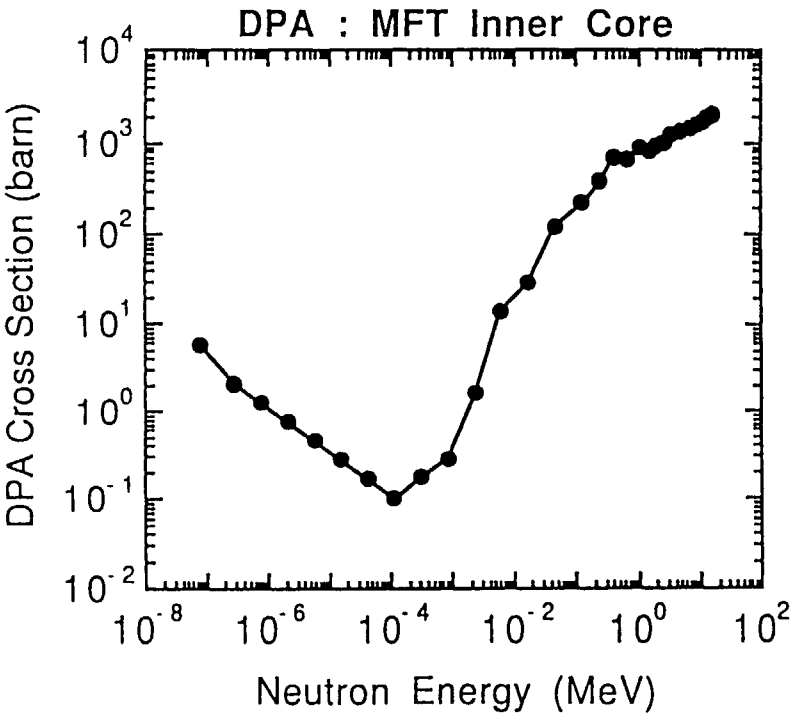

Fig.5.2.4 DPA cross section of MFT inner core

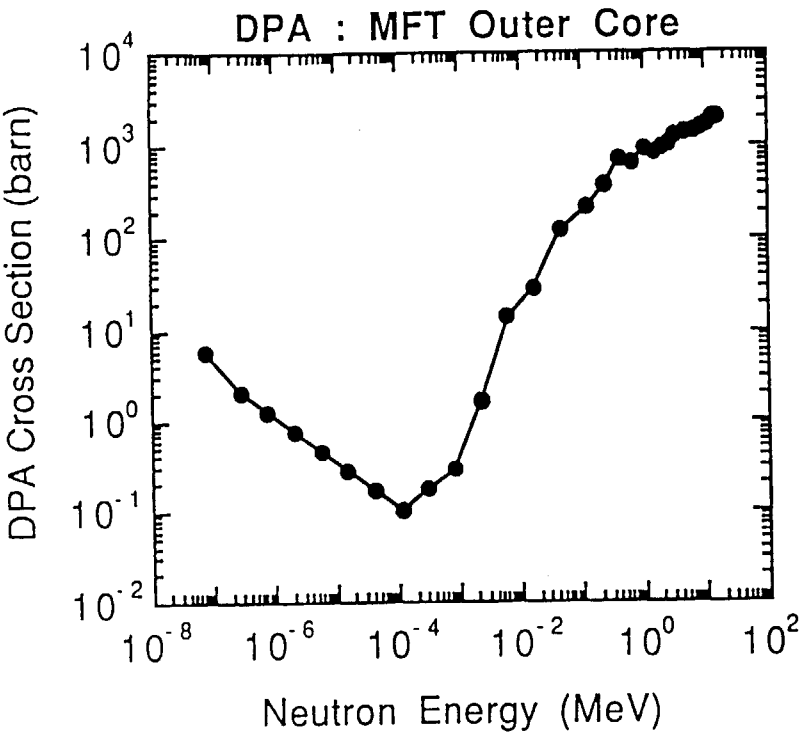

Fig.5.2.5 DPA cross section of MFT outer core

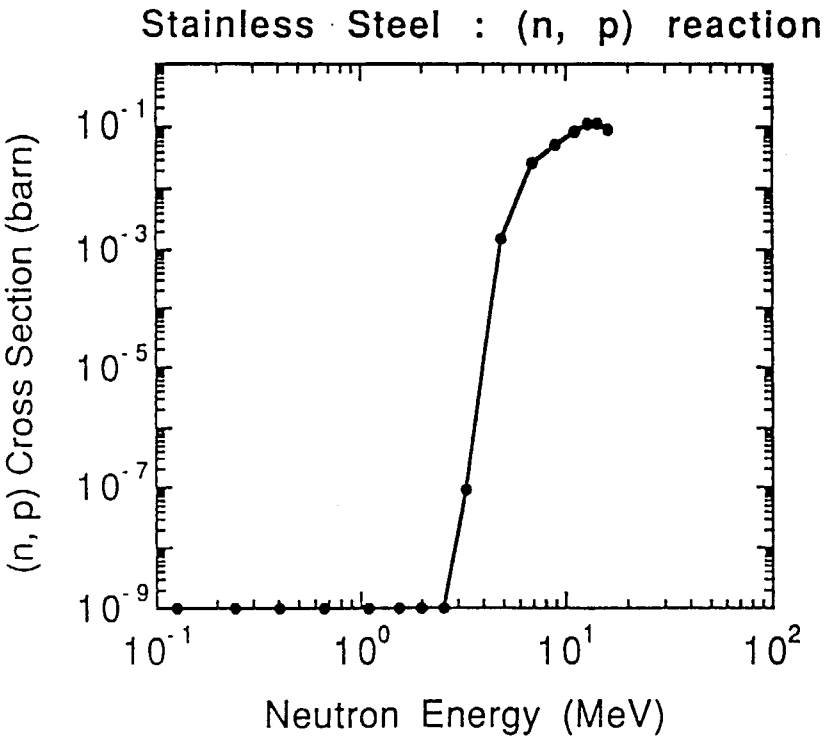

Fig.5.3.1 (n, p) cross section of stainless steel

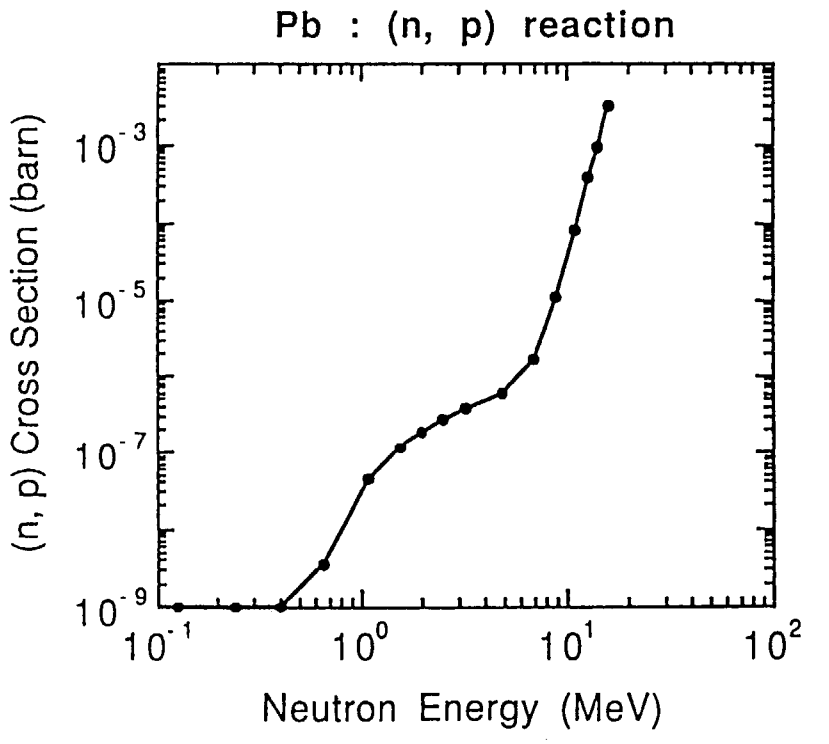

Fig.5.3.2 (n, p) cross section of lead

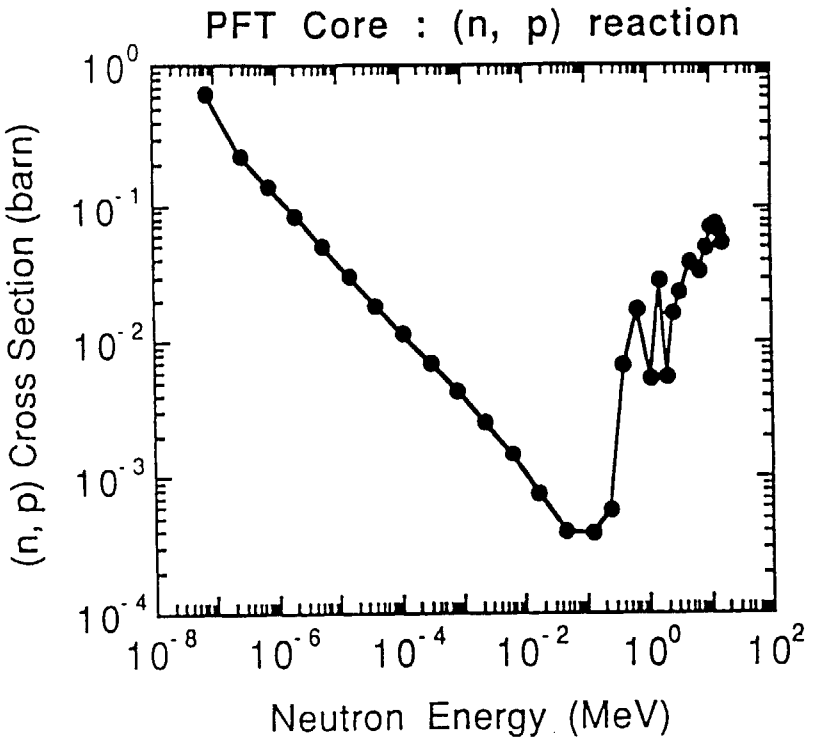

Fig.5.3.3 (n, p) cross section of PFT core

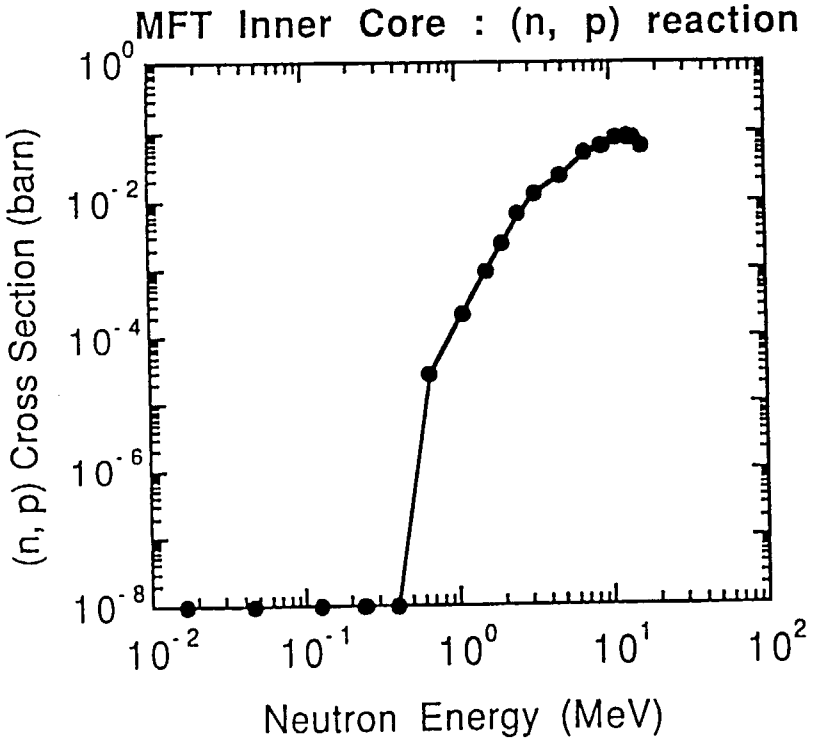

Fig.5.3.4 (n, p) cross section of MFT inner core

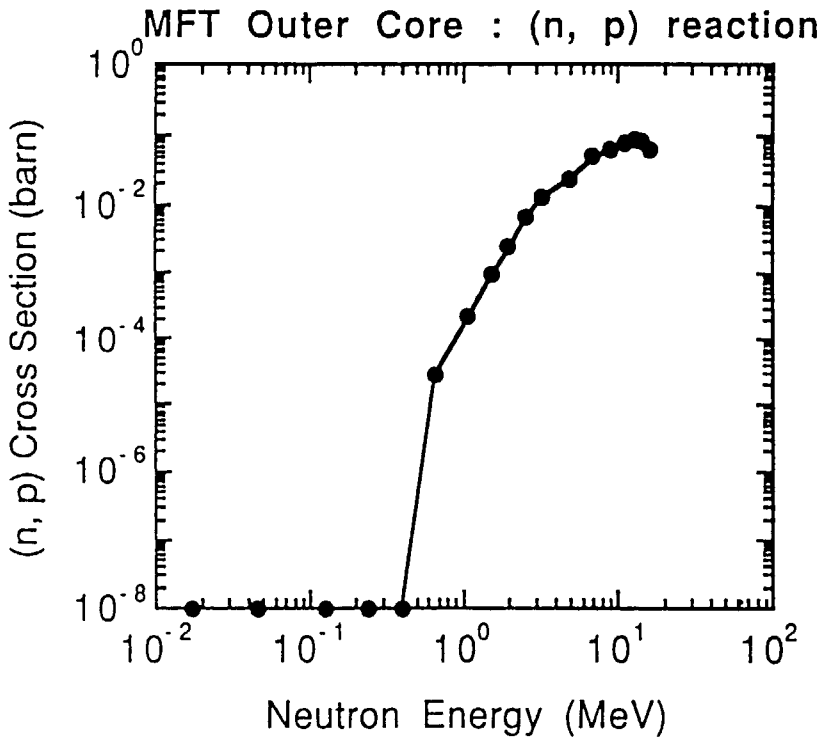

Fig.5.3.5 (n, p) cross section of MFT outer core

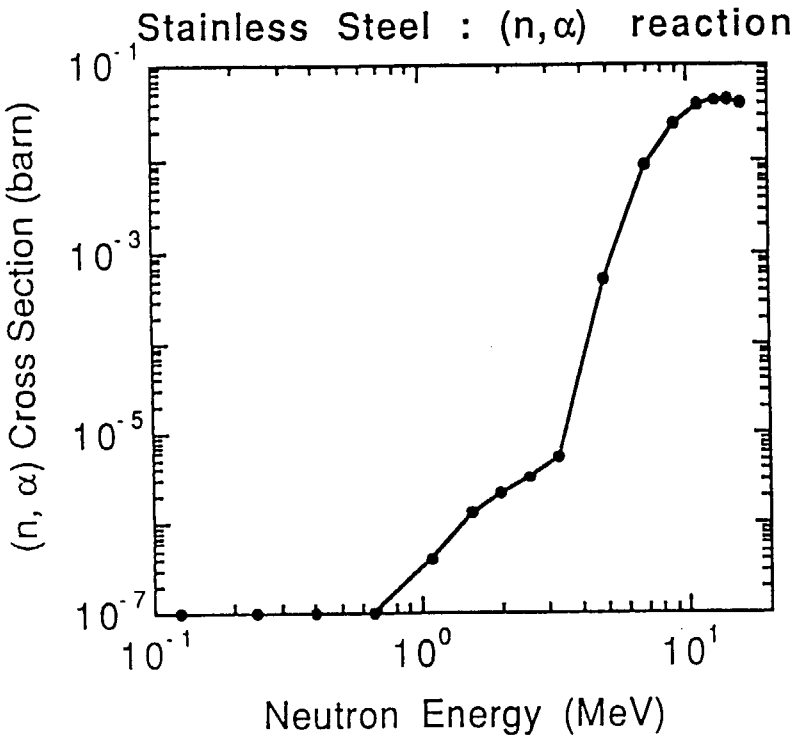

Fig.5.4.1 (n, α) cross section of stainless steel

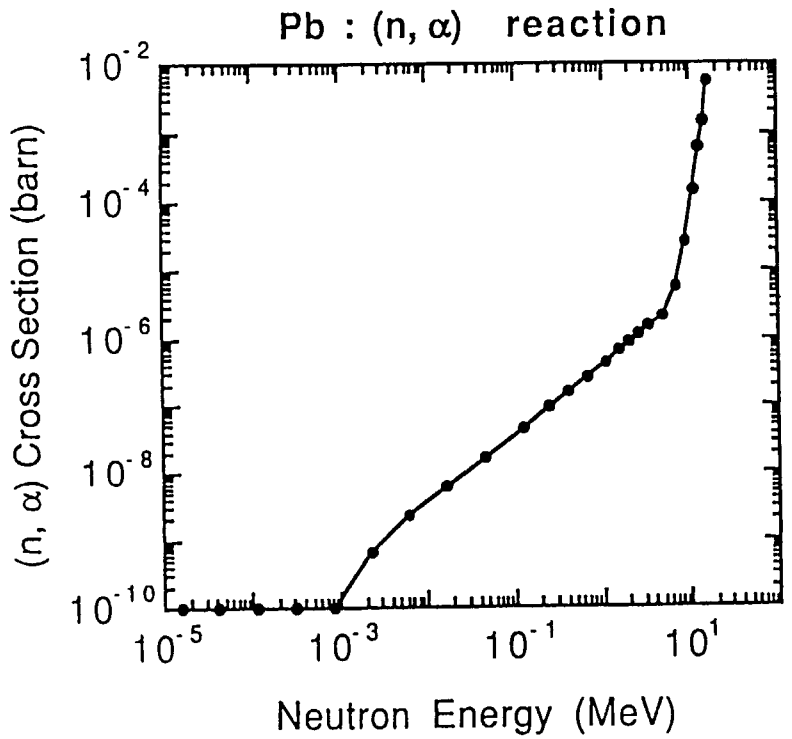

Fig.5.4.2 (n, α) cross section of lead

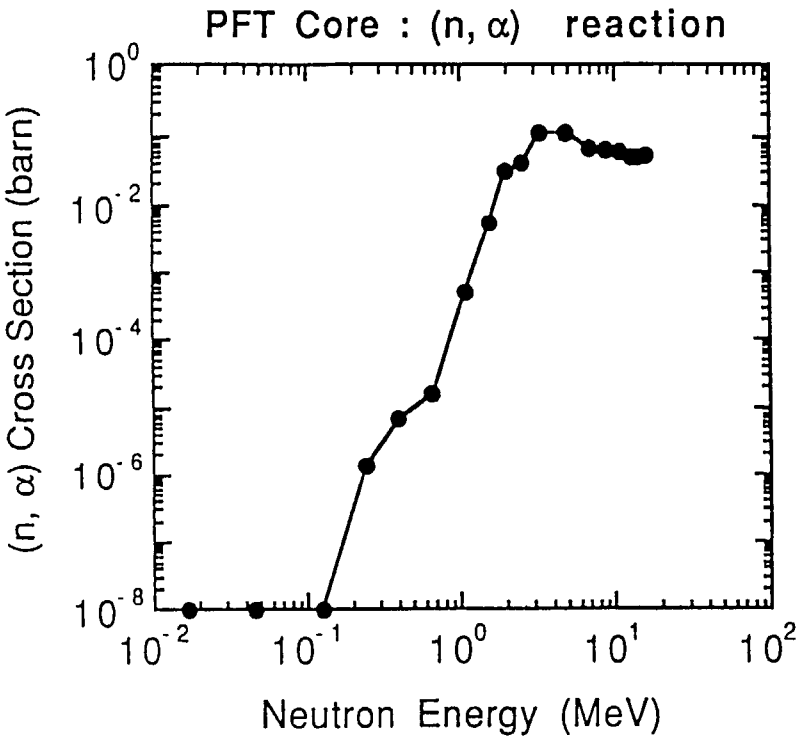

Fig.5.4.3 (n, α) cross section of PFT core

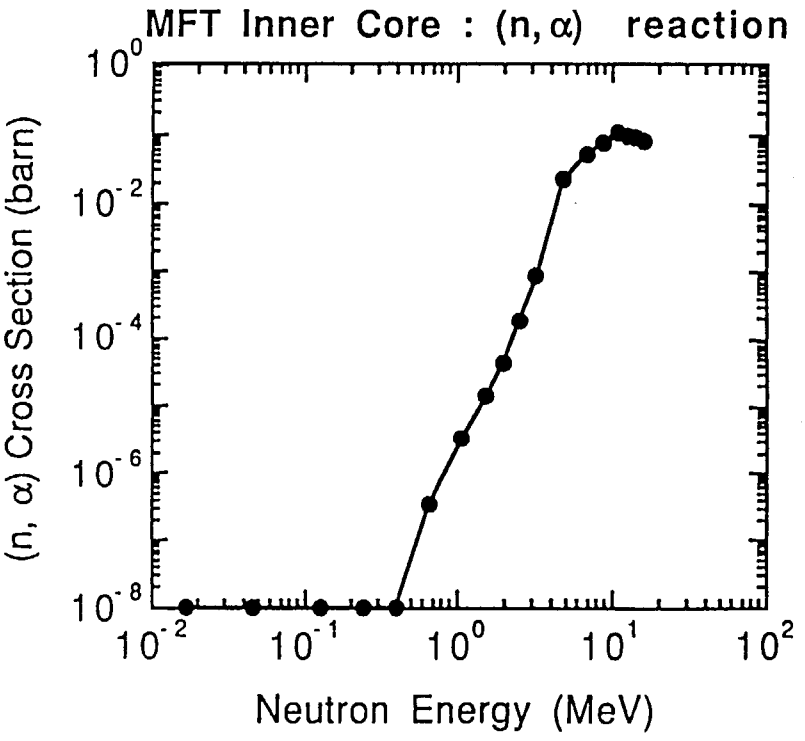

Fig.5.4.4 (n, α) cross section of MFT inner core

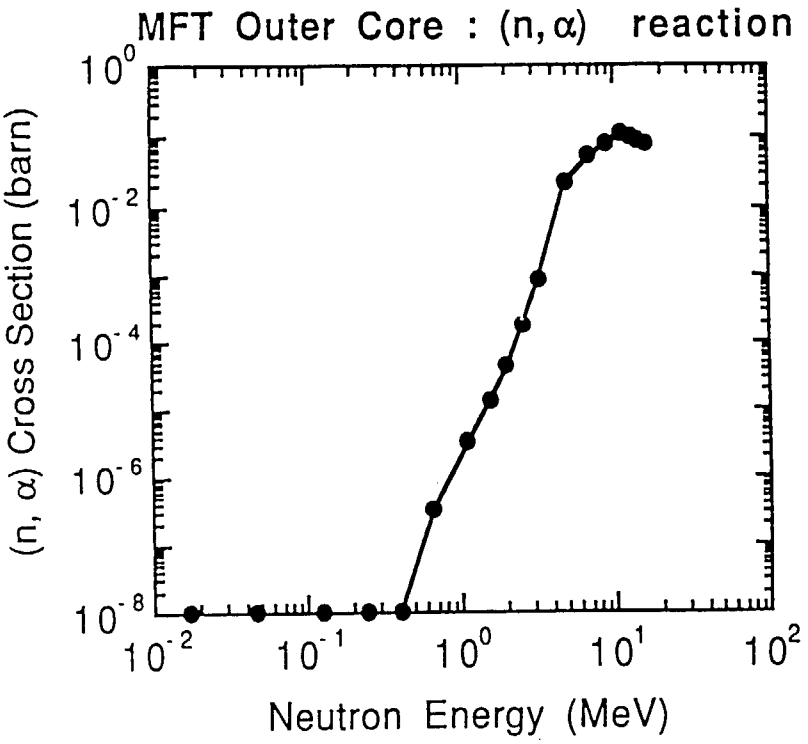

Fig.5.4.5 (n, α) cross section of MFT outer core

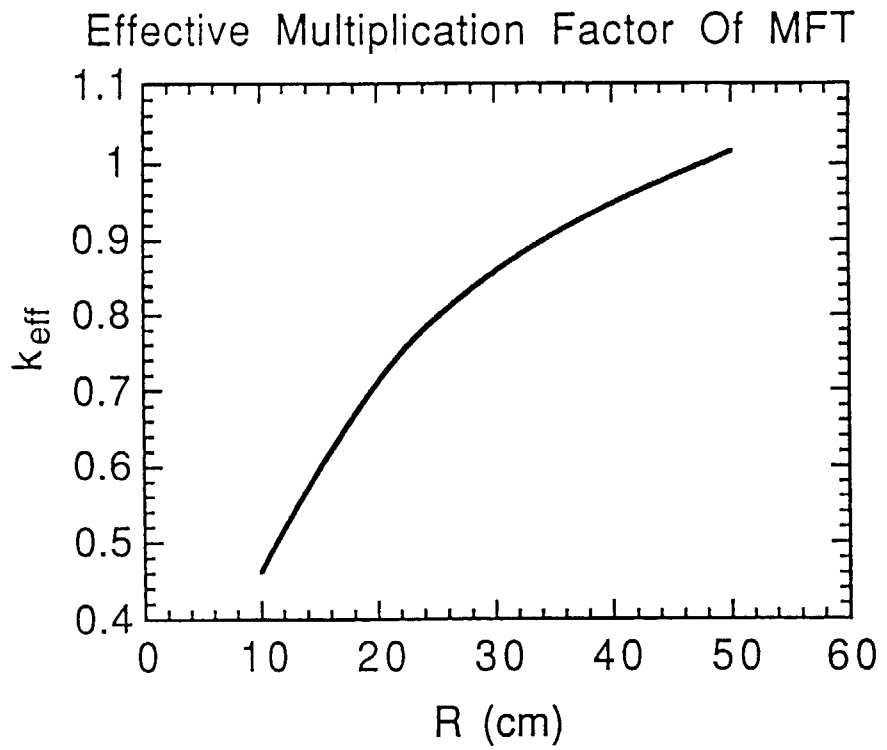

Fig.5.5.1 Effective multiplication factors of MFT

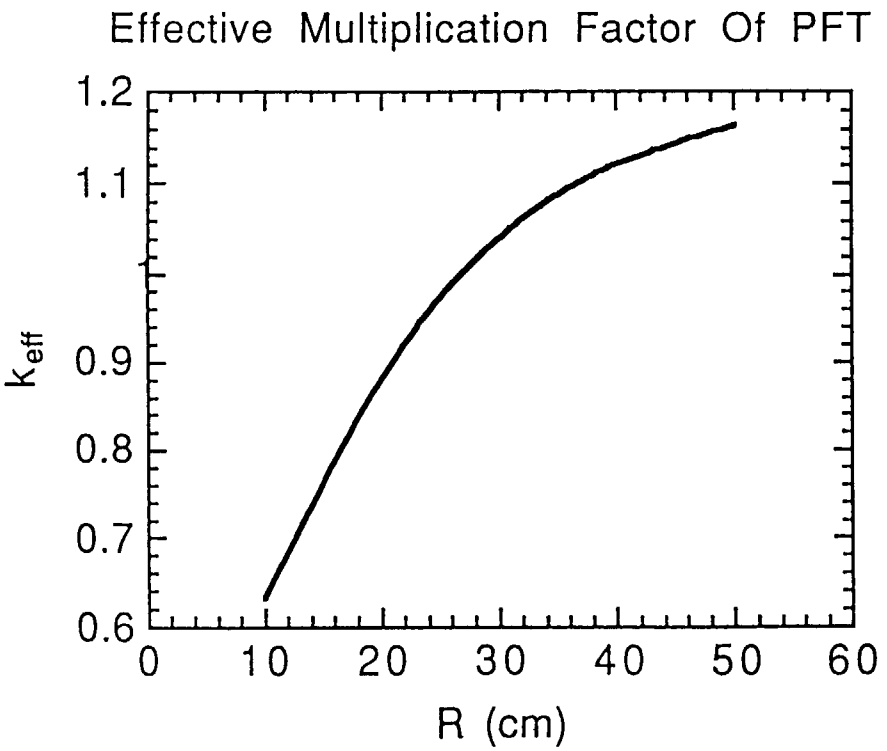

Fig.5.5.2 Effective multiplication factors of PFT

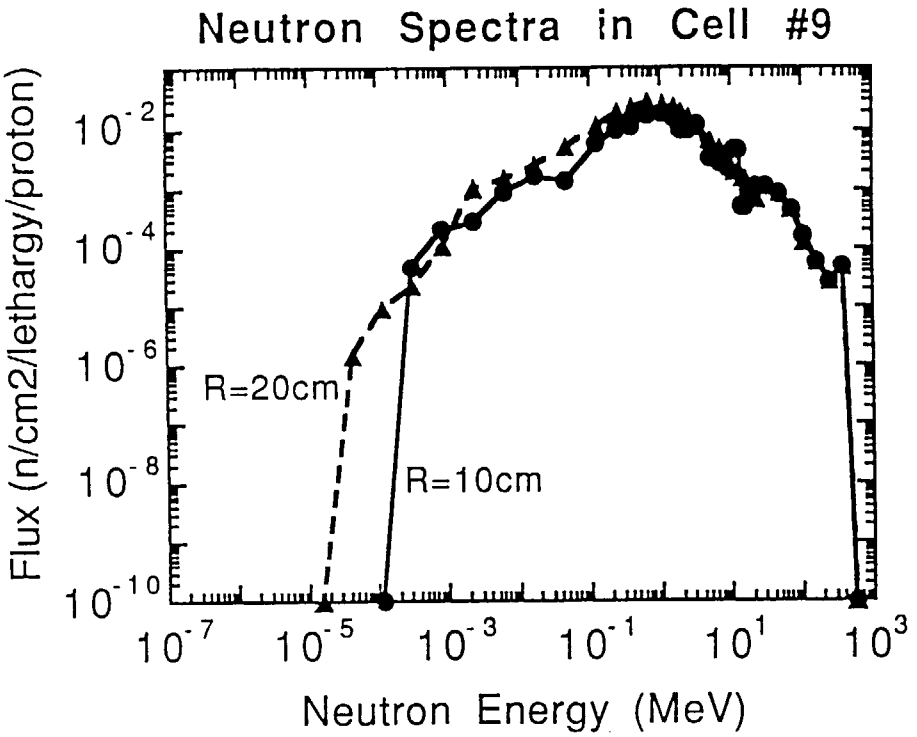

Fig.5.6.1 Neutron spectra in cell #9 of PFT

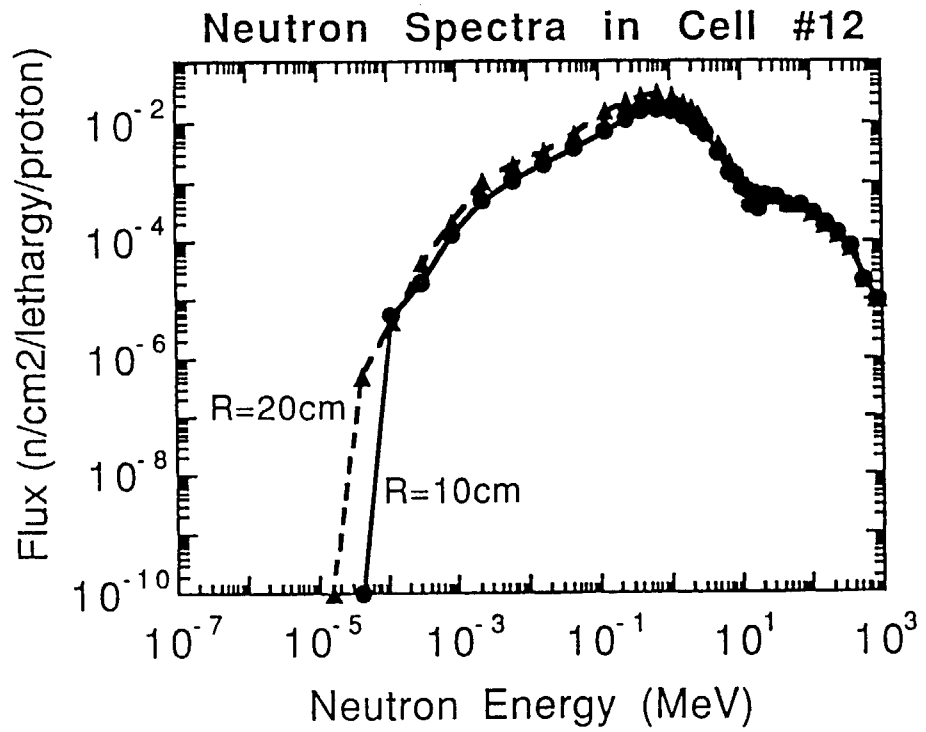

Fig.5.6.2 Neutron spectra in cell #12 of PFT

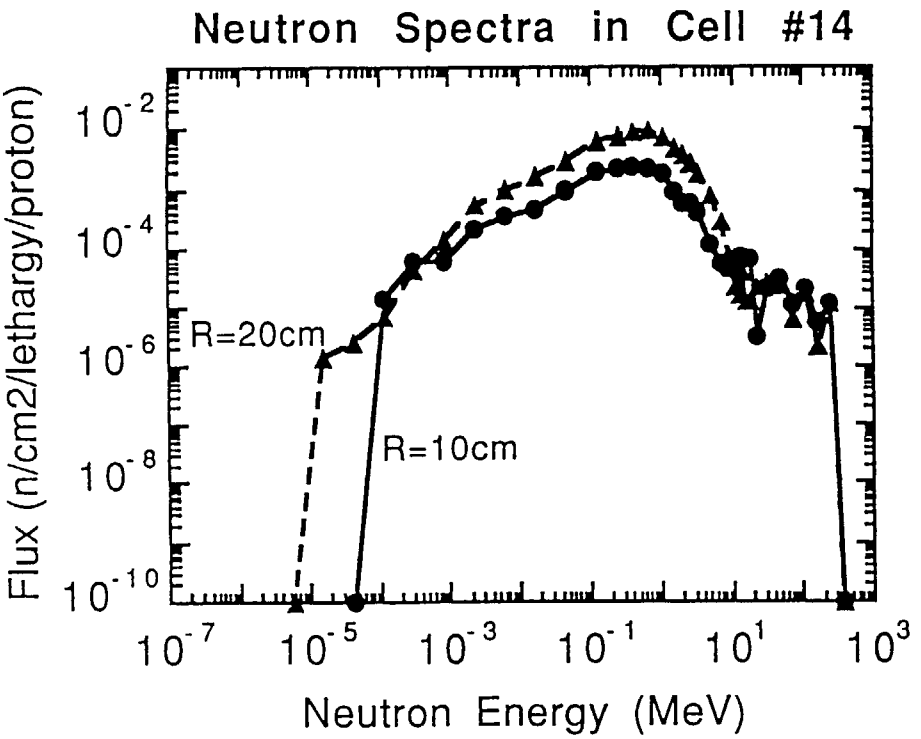

Fig.5.6.3 Neutron spectra in cell #14 of PFT

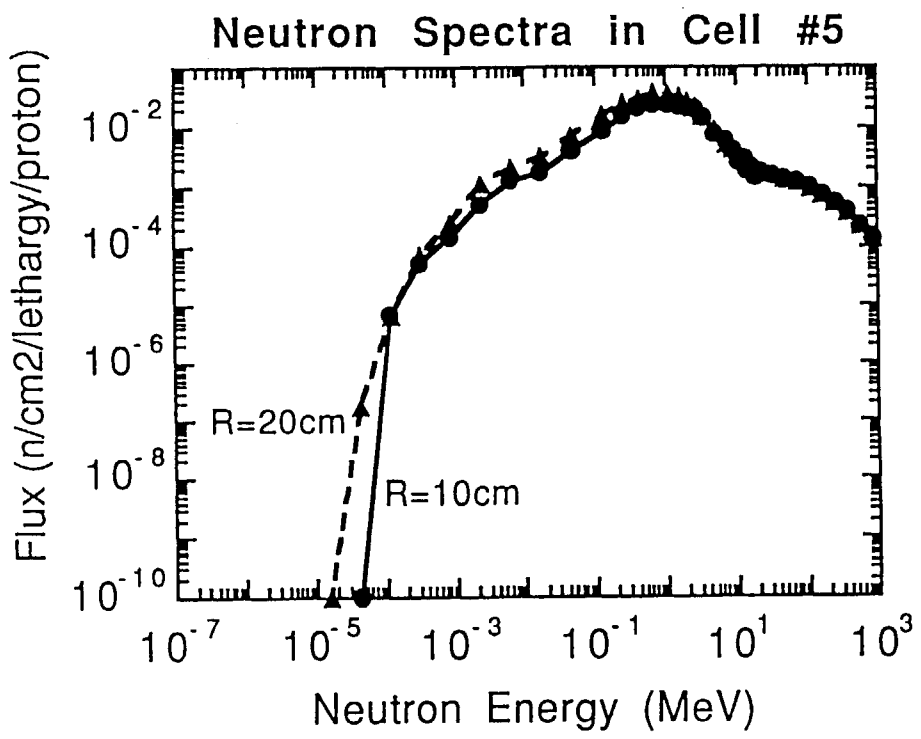

Fig.5.6.4 Neutron spectra in cell #5 of PFT

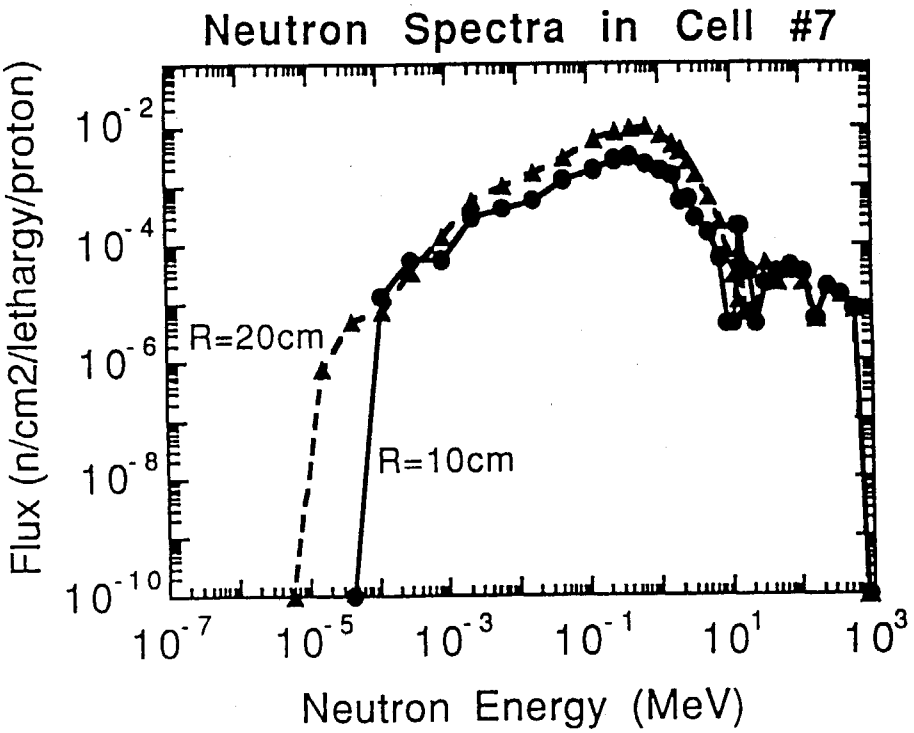

Fig.5.6.5 Neutron spectra in cell #7 of PFT

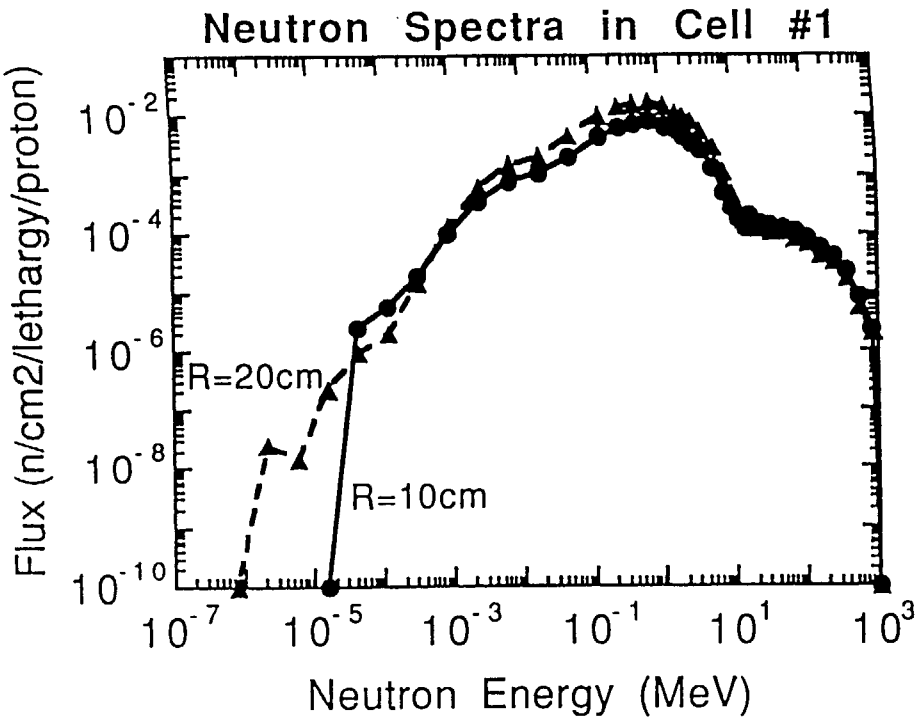

Fig.5.6.6 Neutron spectra in cell #1 of PFT

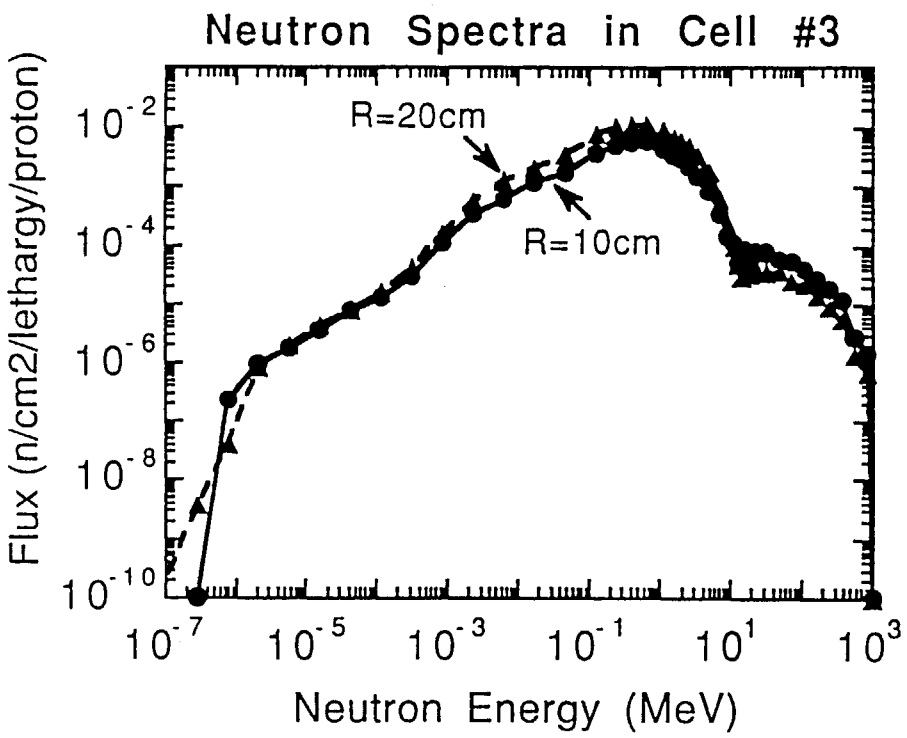

Fig.5.6.7 Neutron spectra in cell #3 of PFT

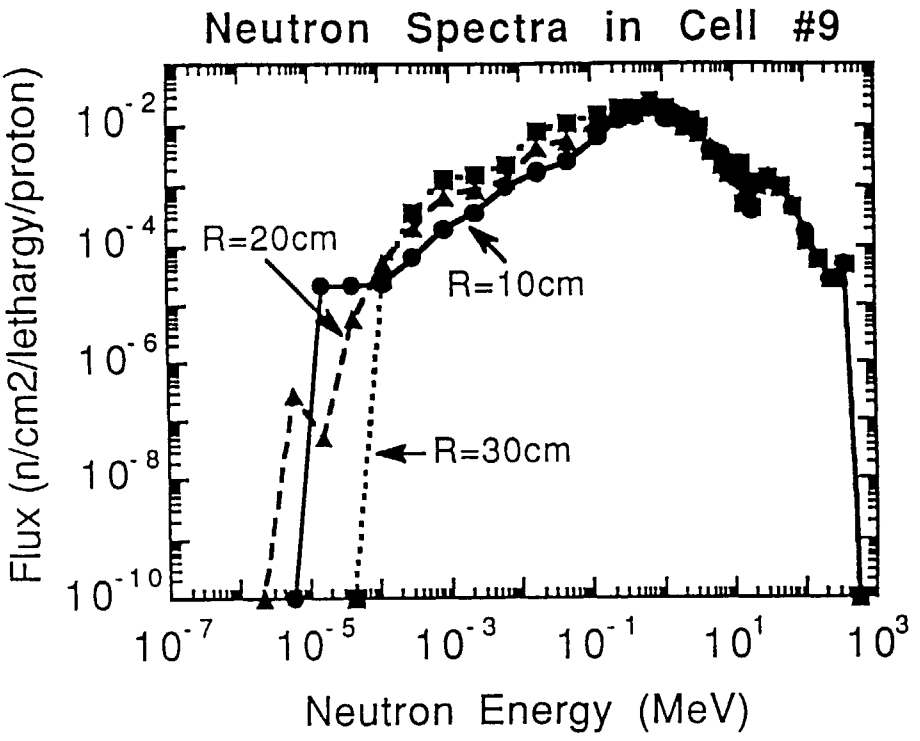

Fig.5.7.1 Neutron spectra in cell #9 of MFT

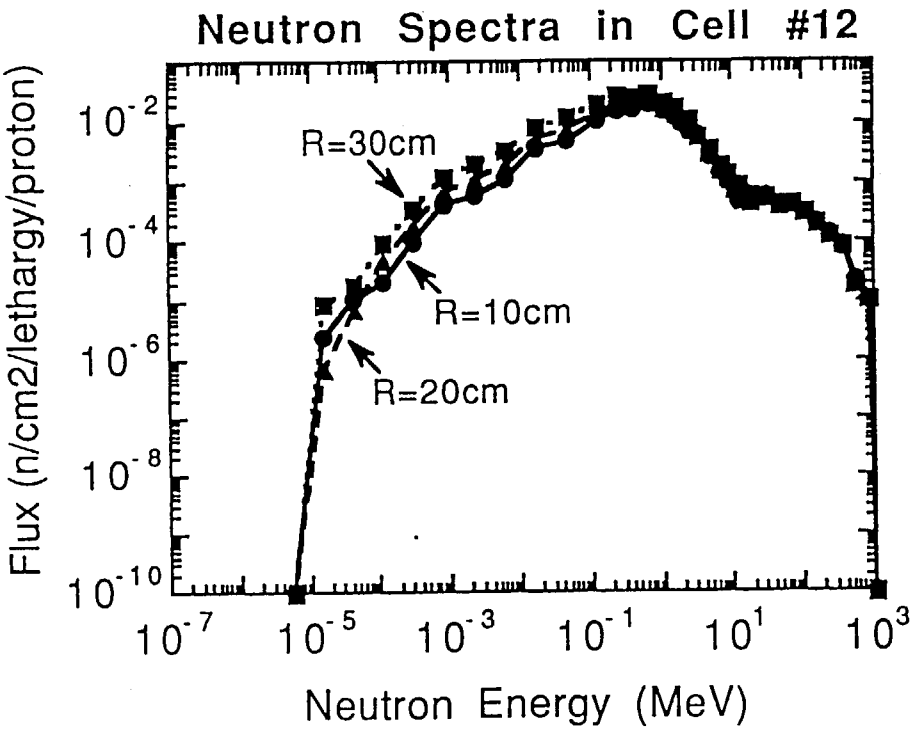

Fig.5.7.2 Neutron spectra in cell #12 of MFT

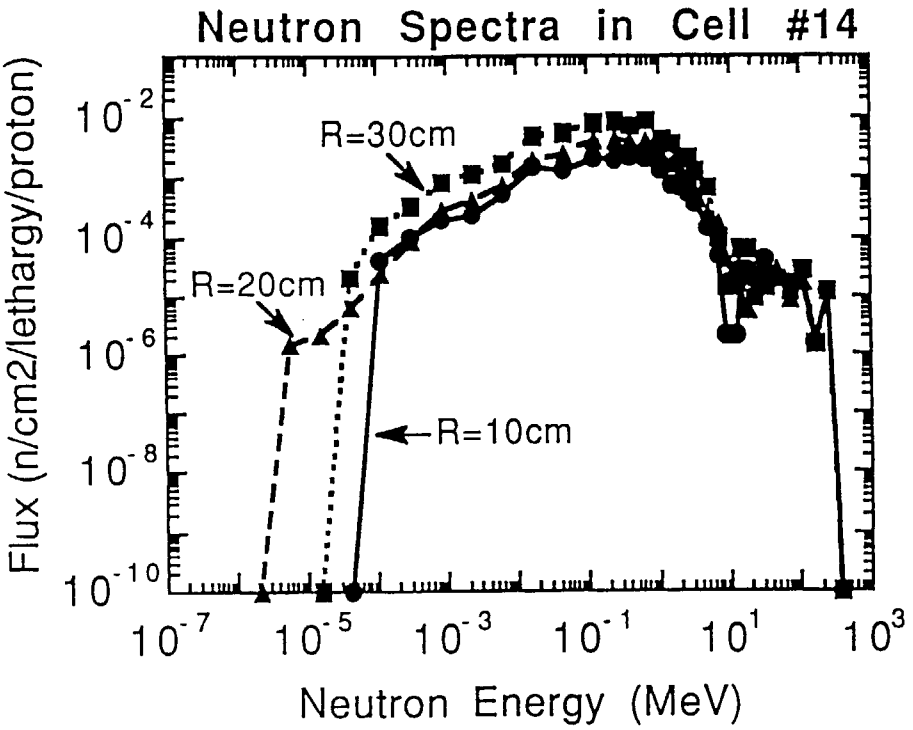

Fig.5.7.3 Neutron spectra in cell #14 of MFT

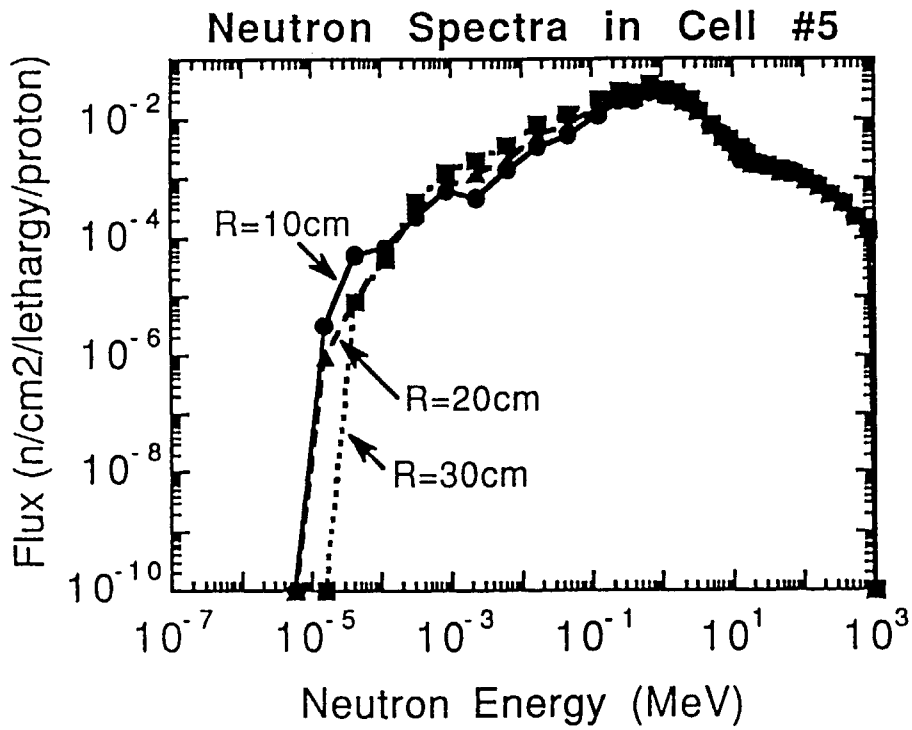

Fig.5.7.4 Neutron spectra in cell #5 of MFT

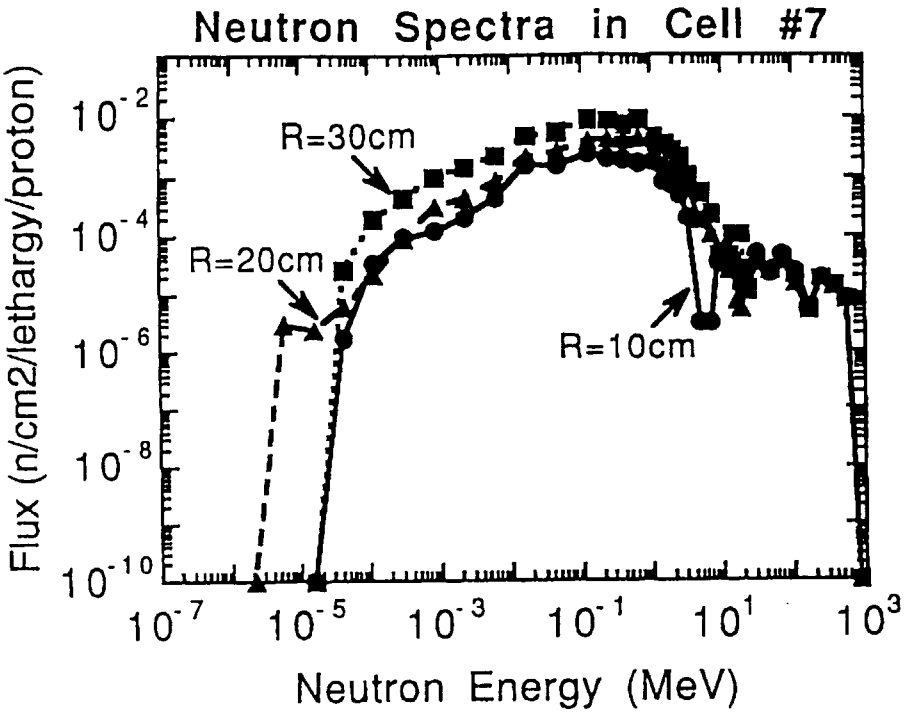

Fig.5.7.5 Neutron spectra in cell #7 of MFT

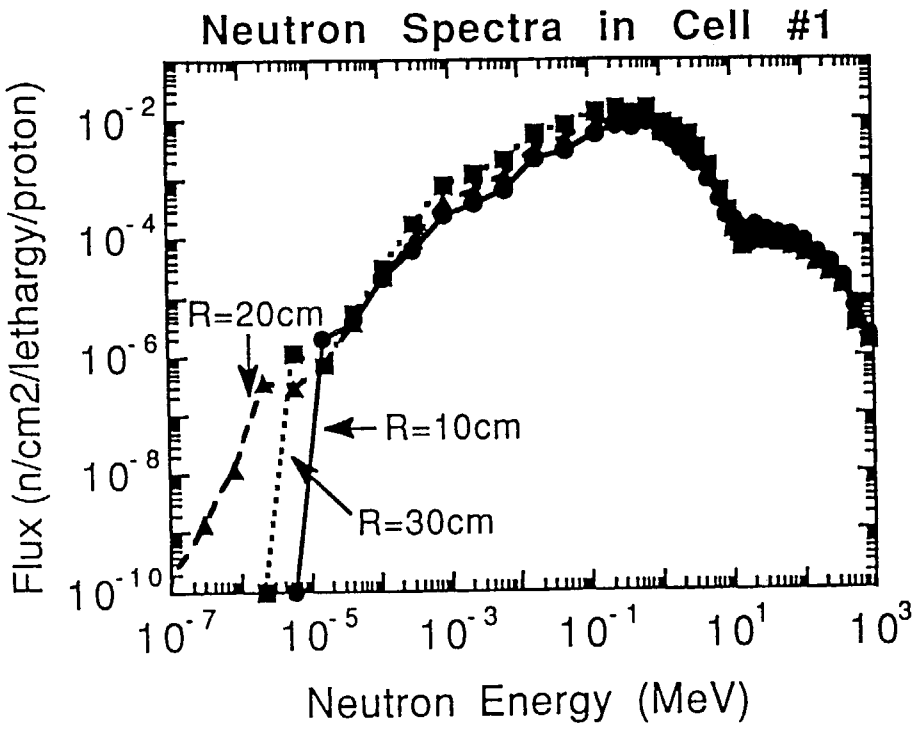

Fig.5.7.6 Neutron spectra in cell #1 of MFT

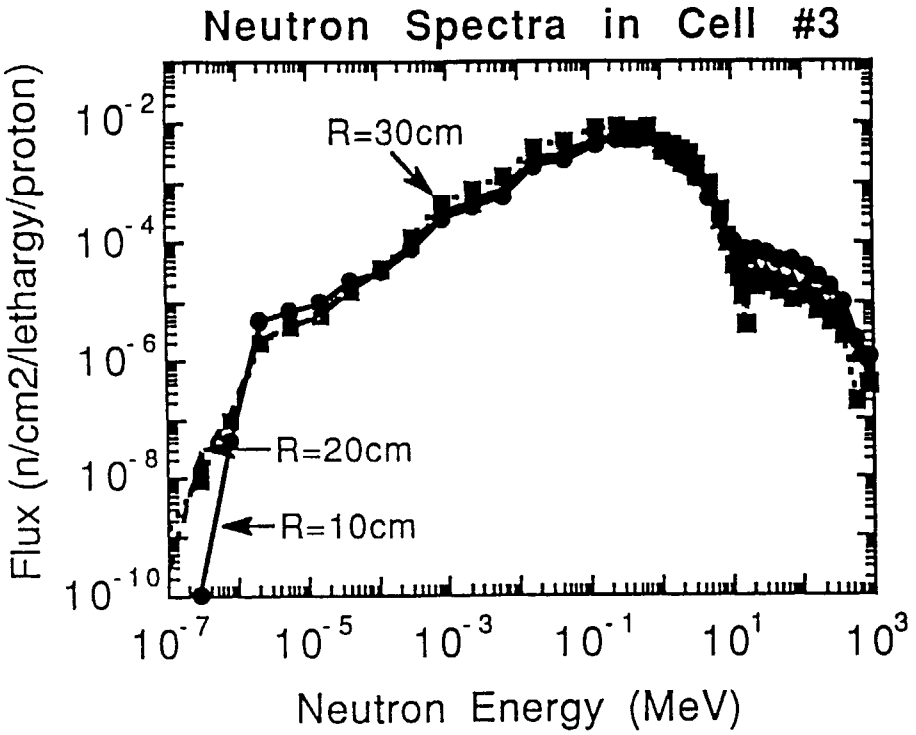

Fig.5.7.7 Neutron spectra in cell #3 of MFT

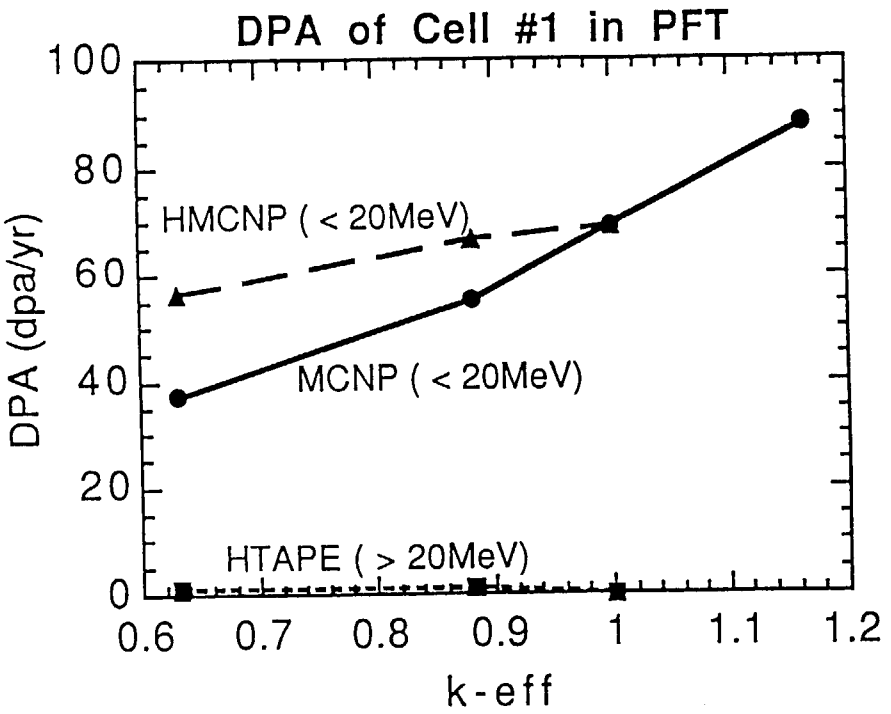

Fig.5.8.1 Annual atomic displacement in cell #1 of PFT

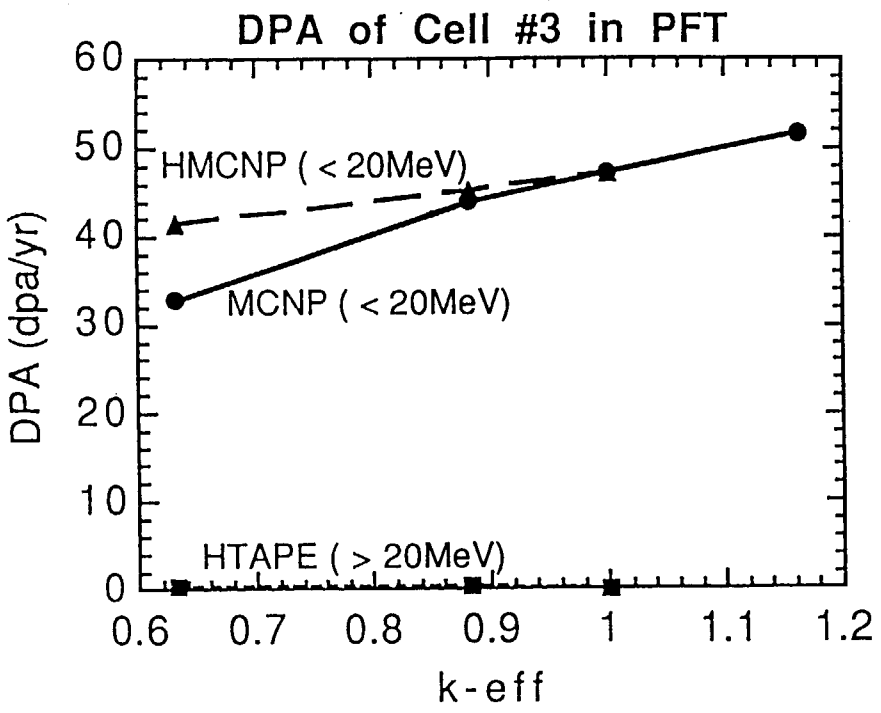

Fig.5.8.2 Annual atomic displacement in cell #3 of PFT

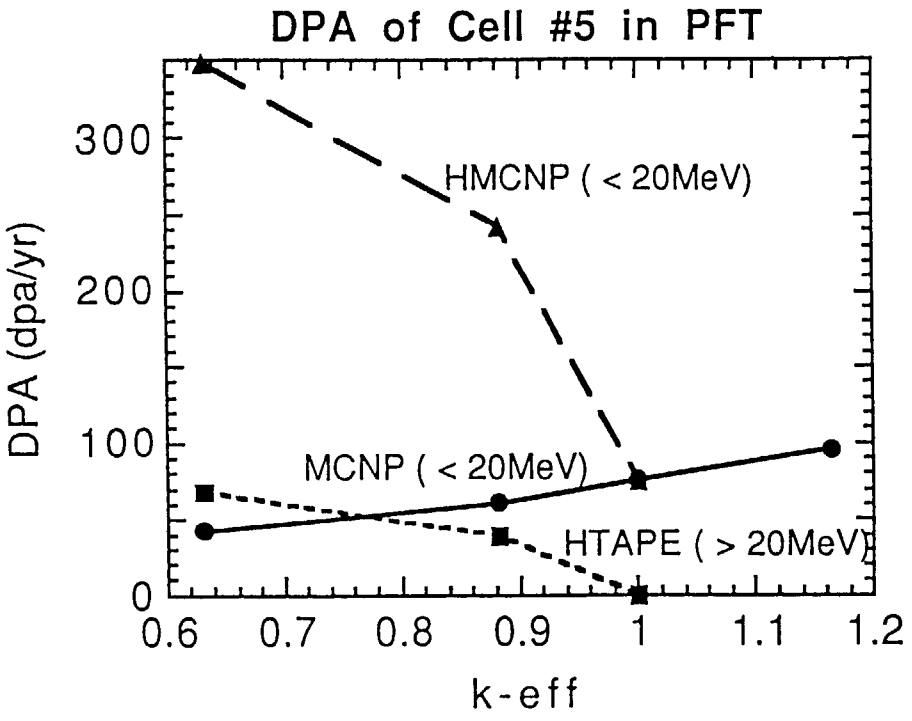

Fig.5.8.3 Annual atomic displacement in cell #5 of PFT

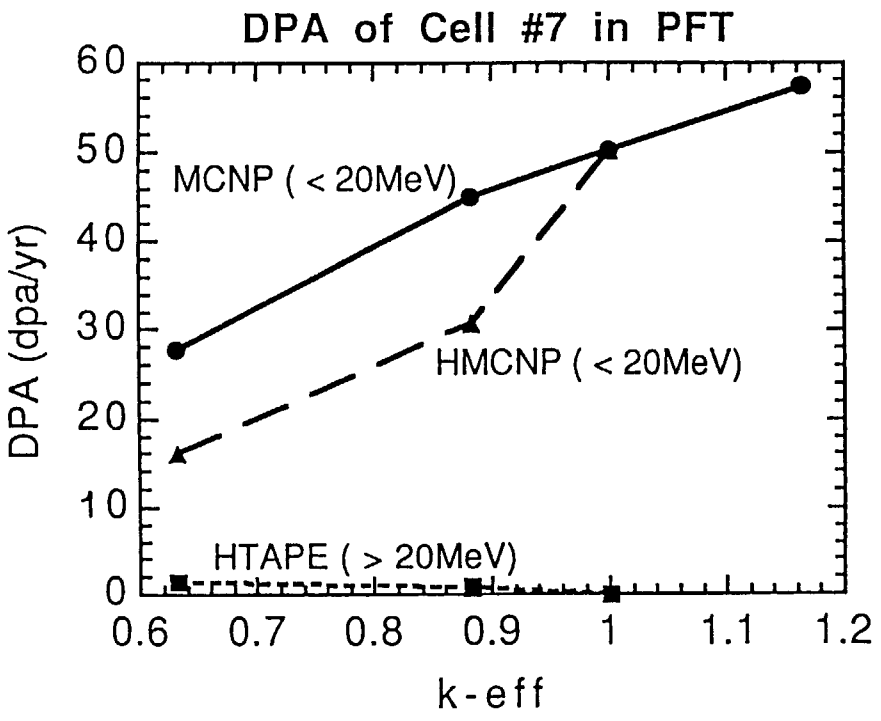

Fig.5.8.4 Annual atomic displacement in cell #7 of PFT

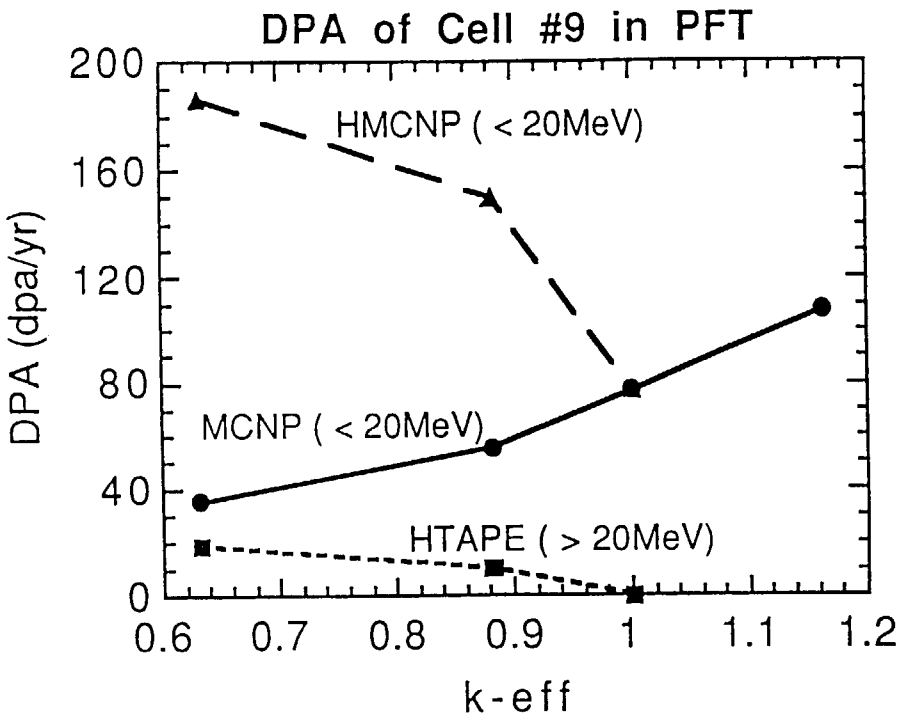

Fig.5.8.5 Annual atomic displacement in cell #9 of PFT

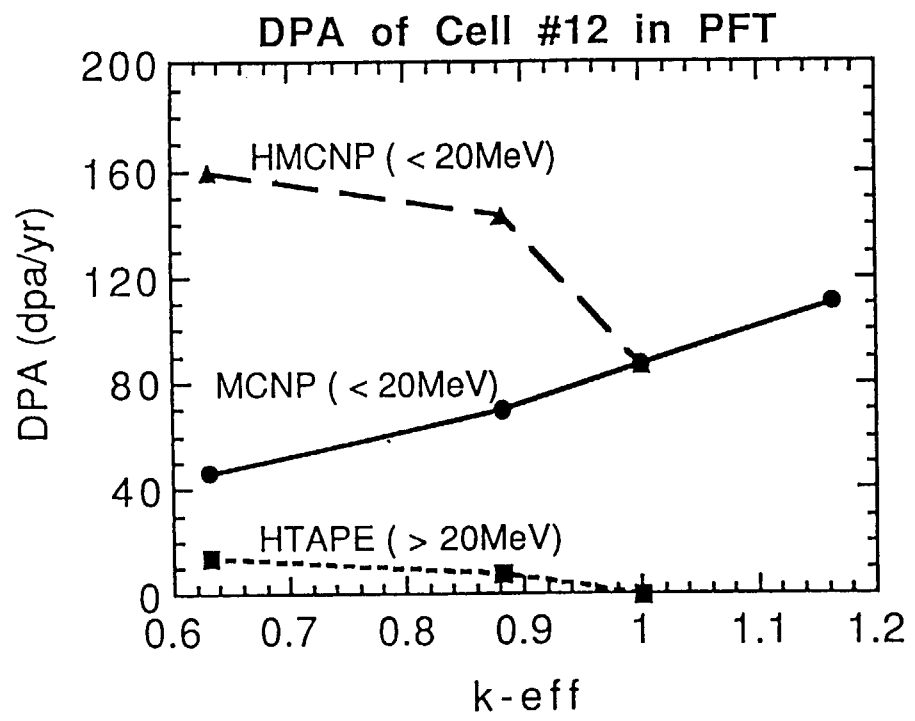

Fig.5.8.6 Annual atomic displacement in cell #12 of PFT

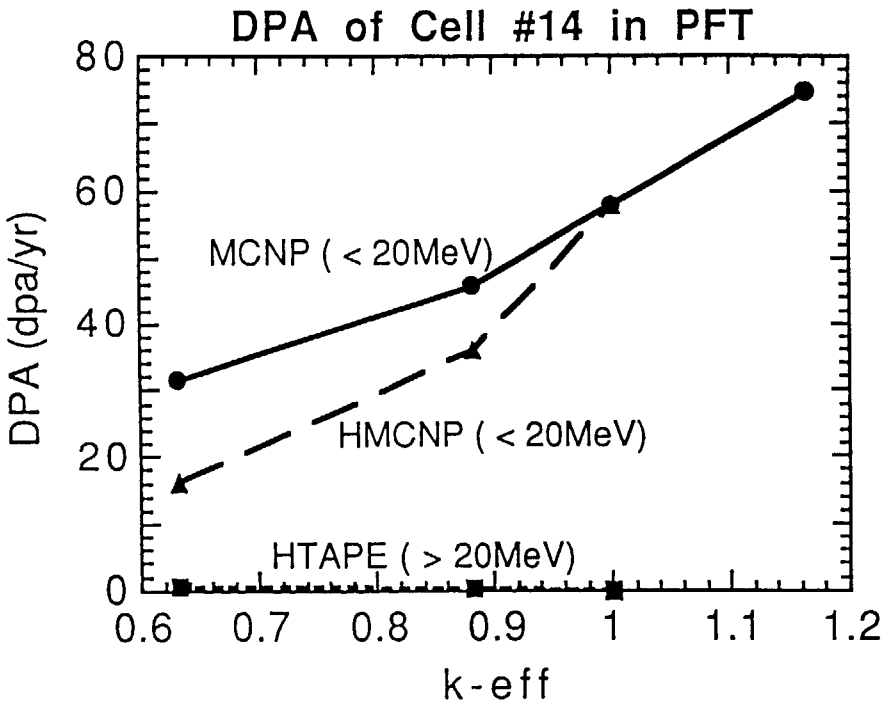

Fig.5.8.7 Annual atomic displacement in cell #14 of PFT

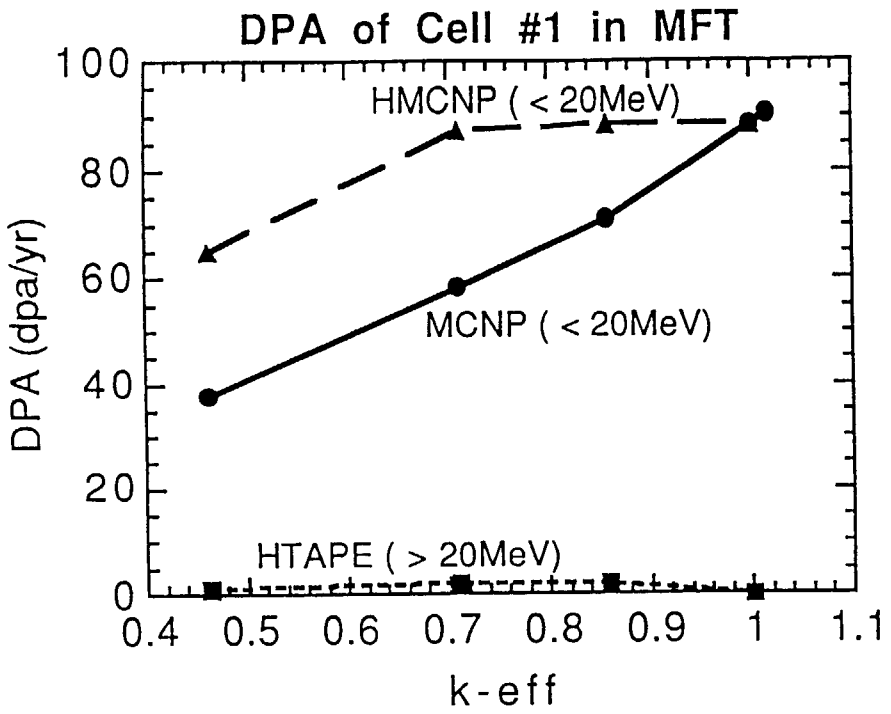

Fig.5.9.1 Annual atomic displacement in cell #1 of MFT

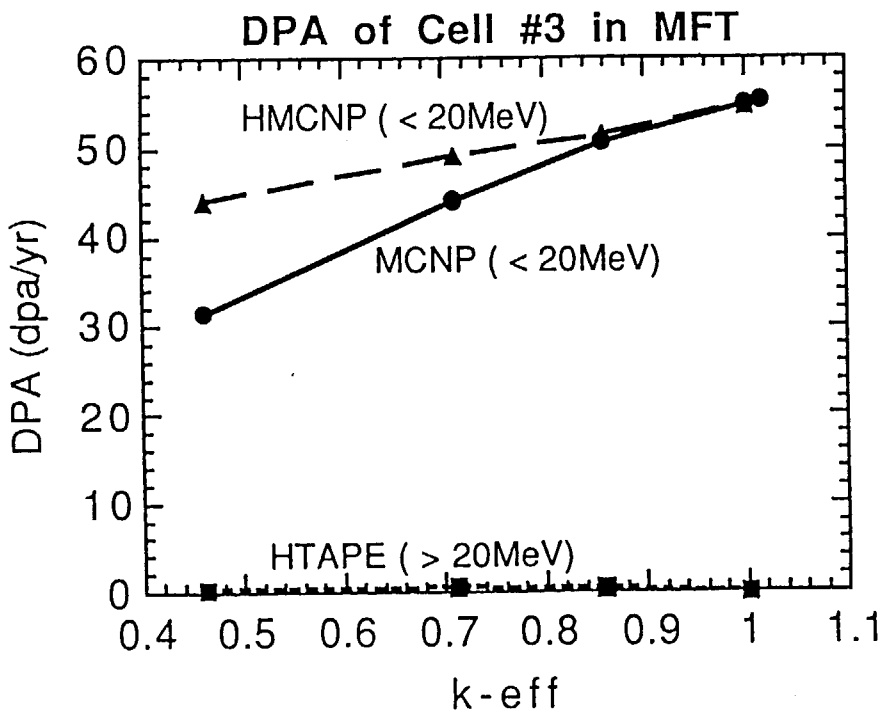

Fig.5.9.2 Annual atomic displacement in cell #3 of MFT

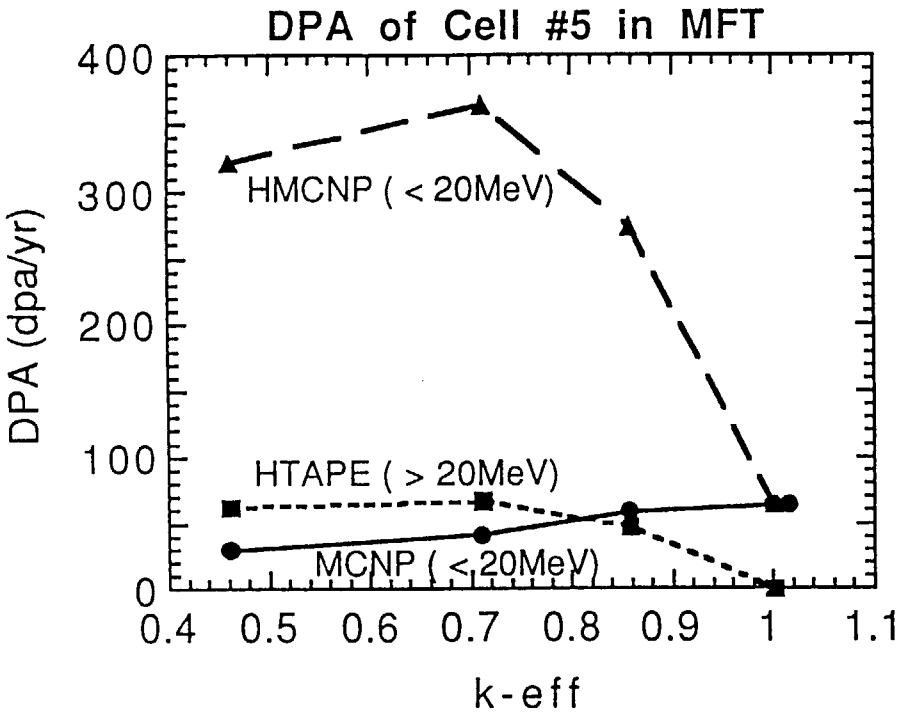

Fig.5.9.3 Annual atomic displacement in cell #5 of MFT

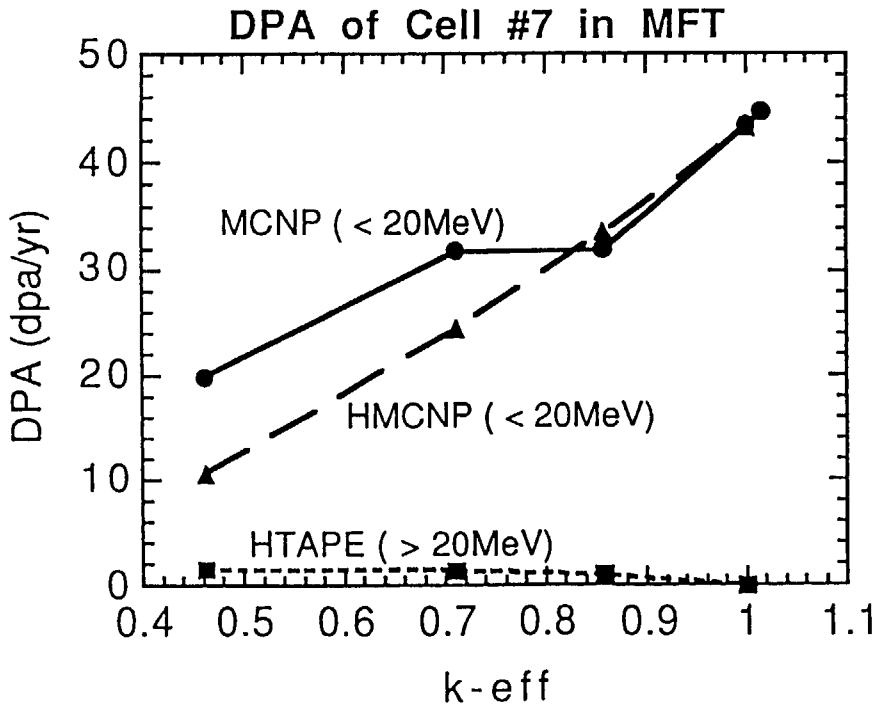

Fig.5.9.4 Annual atomic displacement in cell #7 of MFT

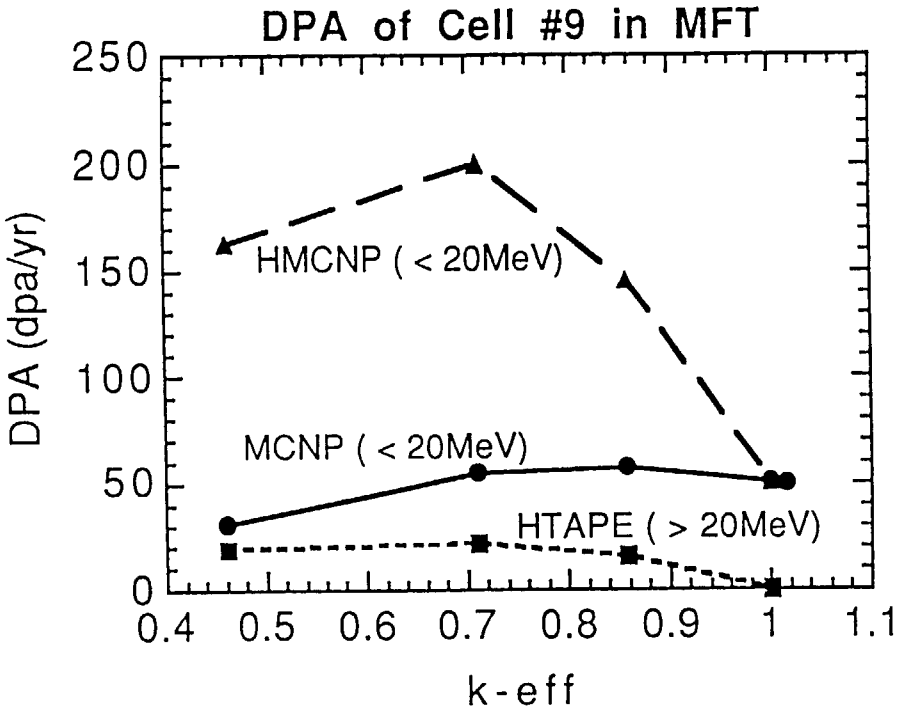

Fig.5.9.5 Annual atomic displacement in cell #9 of MFT

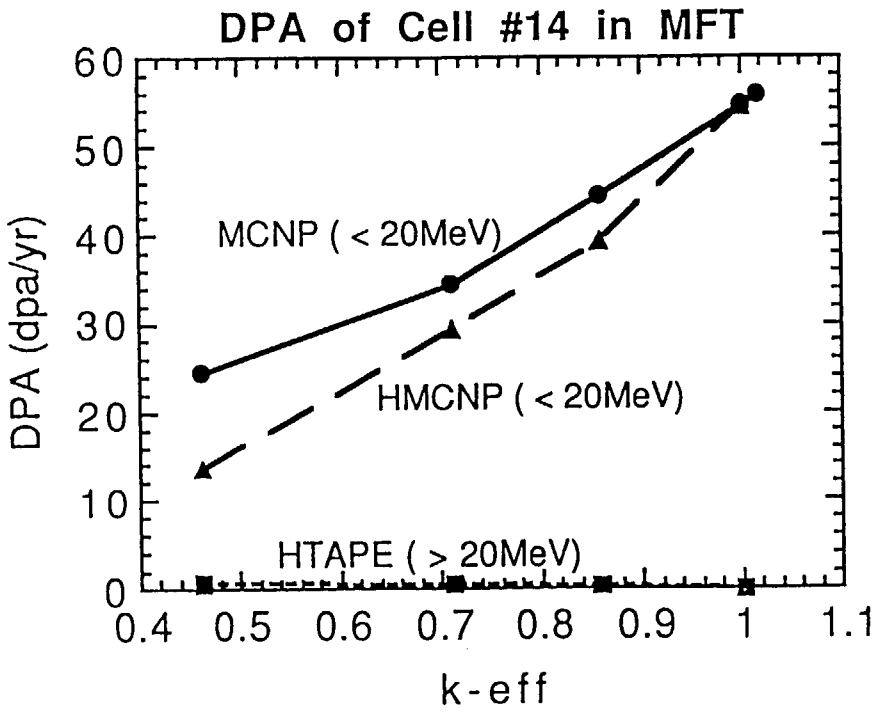

Fig.5.9.6 Annual atomic displacement in cell #14 of MFT

This is a blank page.

国際単位系 (SI) と換算表

表 1　SI 基本単位および補助単位

量	名称	記号
長さ	メートル	m
質量	キログラム	kg
時間	秒	s
電流	アンペア	A
熱力学温度	ケルビン	K
物質量	モル	mol
光度	カンデラ	cd
平面角	ラジアン	rad
立体角	ステラジアン	sr

表 2　SI と併用される単位

名称	記号
分，時，日	min，h，d
度，分，秒	°，′，″
リットル	l，L
トン	t
電子ボルト	eV
原子質量単位	u

1 eV = 1.60218 × 10^{-19} J

1 u = 1.66054 × 10^{-27} kg

表 5　SI 接頭語

倍数	接頭語	記号
10^{18}	エクサ	E
10^{15}	ペタ	P
10^{12}	テラ	T
10^{9}	ギガ	G
10^{6}	メガ	M
10^{3}	キロ	k
10^{2}	ヘクト	h
10^{1}	デカ	da
10^{-1}	デシ	d
10^{-2}	センチ	c
10^{-3}	ミリ	m
10^{-6}	マイクロ	μ
10^{-9}	ナノ	n
10^{-12}	ピコ	p
10^{-15}	フェムト	f
10^{-18}	アト	a

表 3　固有の名称をもつ SI 組立単位

量	名称	記号	他の SI 単位による表現
周波数	ヘルツ	Hz	s^{-1}
力	ニュートン	N	m·kg/s^2
圧力，応力	パスカル	Pa	N/m^2
エネルギー，仕事，熱量	ジュール	J	N·m
工率，放射束	ワット	W	J/s
電気量，電荷	クーロン	C	A·s
電位，電圧，起電力	ボルト	V	W/A
静電容量	ファラド	F	C/V
電気抵抗	オーム	Ω	V/A
コンダクタンス	ジーメンス	S	A/V
磁束	ウェーバ	Wb	V·s
磁束密度	テスラ	T	Wb/m^2
インダクタンス	ヘンリー	H	Wb/A
セルシウス温度	セルシウス度	℃	
光束	ルーメン	lm	cd·sr
照度	ルクス	lx	lm/m^2
放射能	ベクレル	Bq	s^{-1}
吸収線量	グレイ	Gy	J/kg
線量当量	シーベルト	Sv	J/kg

表 4　SI と共に暫定的に維持される単位

名称	記号
オングストローム	Å
バーン	b
バール	bar
ガル	Gal
キュリー	Ci
レントゲン	R
ラド	rad
レム	rem

1 Å = 0.1 nm = 10^{-10} m

1 b = 100 fm^2 = 10^{-28} m^2

1 bar = 0.1 MPa = 10^5 Pa

1 Gal = 1 cm/s^2 = 10^{-2} m/s^2

1 Ci = 3.7 × 10^{10} Bq

1 R = 2.58 × 10^{-4} C/kg

1 rad = 1 cGy = 10^{-2} Gy

1 rem = 1 cSv = 10^{-2} Sv

（注）

1. 表 1　5 は「国際単位系」第 5 版，国際度量衡局 1985 年刊行による。ただし，1 eV および 1 u の値は CODATA の 1986 年推奨値によった。
2. 表 4 には海里，ノット，アール，ヘクタールも含まれているが日常の単位なのでここでは省略した。
3. bar は，JIS では流体の圧力を表わす場合に限り表 2 のカテゴリーに分類されている。
4. EC 閣僚理事会指令では bar，barn および「血圧の単位」mmHg を表 2 のカテゴリーに入れている。

換　算　表

力	N(=10^5 dyn)	kgf	lbf
	1	0.101972	0.224809
	9.80665	1	2.20462
	4.44822	0.453592	1

粘度　1 Pa·s(N·s/m^2) = 10 P(ポアズ)(g/(cm·s))

動粘度　1 m^2/s = 10^4 St(ストークス)(cm^2/s)

圧力	MPa(=10 bar)	kgf/cm^2	atm	mmHg(Torr)	lbf/in^2(psi)
	1	10.1972	9.86923	7.50062 × 10^3	145.038
	0.0980665	1	0.967841	735.559	14.2233
	0.101325	1.03323	1	760	14.6959
	1.33322 × 10^{-4}	1.35951 × 10^{-3}	1.31579 × 10^{-3}	1	1.93368 × 10^{-2}
	6.89476 × 10^{-3}	7.03070 × 10^{-2}	6.80460 × 10^{-2}	51.7149	1

エネルギー・仕事・熱量	J(=10^7 erg)	kgf·m	kW·h	cal(計量法)	Btu	ft·lbf	eV
	1	0.101972	2.77778 × 10^{-7}	0.238889	9.47813 × 10^{-4}	0.737562	6.24150 × 10^{18}
	9.80665	1	2.72407 × 10^{-6}	2.34270	9.29487 × 10^{-3}	7.23301	6.12082 × 10^{19}
	3.6 × 10^6	3.67098 × 10^5	1	8.59999 × 10^5	3412.13	2.65522 × 10^6	2.24694 × 10^{25}
	4.18605	0.426858	1.16279 × 10^{-6}	1	3.96759 × 10^{-3}	3.08747	2.61272 × 10^{19}
	1055.06	107.586	2.93072 × 10^{-4}	252.042	1	778.172	6.58515 × 10^{21}
	1.35582	0.138255	3.76616 × 10^{-7}	0.323890	1.28506 × 10^{-3}	1	8.46233 × 10^{18}
	1.60218 × 10^{-19}	1.63377 × 10^{-20}	4.45050 × 10^{-26}	3.82743 × 10^{-20}	1.51857 × 10^{-22}	1.18171 × 10^{-19}	1

1 cal = 4.18605 J (計量法)
= 4.184 J (熱化学)
= 4.1855 J (15 °C)
= 4.1868 J (国際蒸気表)

仕事率　1 PS (仏馬力)
= 75 kgf·m/s
= 735.499 W

放射能	Bq	Ci
	1	2.70270 × 10^{-11}
	3.7 × 10^{10}	1

吸収線量	Gy	rad
	1	100
	0.01	1

照射線量	C/kg	R
	1	3876
	2.58 × 10^{-4}	1

線量当量	Sv	rem
	1	100
	0.01	1

(86 年 12 月 26 日現在)

THE EVALUATION OF RADIATION DAMAGE TO THE TARGET MATERIAL DUE TO THE INJECTION OF MEDIUM-AND HIGH-ENERGY PROTON